UNIVERSITY OF CALIFORNIA
SANTA CRUZ

COMPARATIVE REGIONAL HYDROLOGIC CHANGES DURING THE EARLY EOCENE

A dissertation submitted in partial satisfaction
of the requirements for the degree of

DOCTOR OF PHILOSOPHY

in

EARTH AND PLANETARY SCIENCES

by

William D. Rush

September 2022

The Dissertation of William D. Rush is approved:

_____
Professor James C. Zachos, Chair

_____
Professor Terrence Blackburn

_____
Professor Noah Finnegan

_____
Professor Pratigya Polissar

_____
Peter Biehl
Vice Provost and Dean of Graduate Studies

Table of Contents

List of Figures

Abstract

Comparative Regional Hydrologic Changes During the Early Eocene

William Rush

The early Eocene is punctuated by a series of rapid warming events, known as hyperthermals. The first among these, the Paleocene-Eocene Thermal Maximum, or PETM, has been argued to be one of the closest approximations to modern-day, anthropogenic warming in the geologic record. The PETM, and the subsequent hyperthermals of smaller magnitude, such as Eocene Thermal Maximum 2, or ETM2, can provide insight into our future warmer world. In addition to temperature changes, these hyperthermals drove significant changes in regional precipitation patterns. This study seeks to better understand these changes, focusing on the mid-latitude North Atlantic coasts, utilizing a suite of techniques including high-resolution climate models and geochemical, sedimentological, and paleoecological proxies. Our models show a significant increase in the seasonality and extremes of precipitation in response to elevated CO_2 levels, with significant differences regionally depending upon orbital configuration. In the western Mid-Atlantic we find a dramatic weathering response to these precipitation changes, with an increase both in chemical alteration and physical transport of sediment. During ETM2, in contrast to studies in other regions, the climatic response was much more muted, with temperatures decreasing, a moderate increase in chemical weathering, and little response in the marine palynology, highlighting the importance climatic forcings apart from CO_2 such as orbital forcing and dynamic feedbacks.

Acknowledgements

I would first like to thank my advisor James Zachos for his support and direction through the course of my doctorate and for bringing me in to the paleoclimate community. To that end, I would also like to thank Christine Shields, Jeff Kiehl, and Mark Snyder for teaching me everything I know about climate modeling. I would like to thank Jean Self-Trail and Marci Robinson who provided me with materials as well as invaluable knowledge on the sediments of the Mid-Atlantic Coast. This was a collaborative project and could not have been completed with the work of Philip Pogge von Strandmann who provided lithium isotope measurements, Appy Sluijs who measured TEX_{86} values, Henk Brinkhuis who provided palynological counts, and Wendy Zhang who performed paleomagnetic analysis. On the note of analysis, I would also like to thank our wonderful technical staff in the EPS department, including Brian Dreyer, Brandon Cheney, and Colin Carney who assisted in the development of the methods for this project. I would also like to thank the rest of my dissertation committee including Terry Blackburn, Pratigya Polissar, and Noah Finnegan who helped me see this project through. Finally, I would like to thank my lab mates through the years who have helped with this project including Dustin Harper, Daisy Zhang, Jo Holo, and Simin Jin.

The text of this dissertation includes a reprint of the following previously published material: Rush, W.D., Kiehl, J.T., Shields, C.A. and Zachos, J.C., 2021. Increased frequency of extreme precipitation events in the North Atlantic during the PETM: Observations and theory. Palaeogeography, Palaeoclimatology, Palaeoecology, 568, p.110289. Mathew Rothstein and Mark Snyder contributed to model construct. Funding for this project was provided by a Heising-Simons Foundation Grant to JTK, an NSF grant (OCE-1415958) to JCZ and the Ida

Benson Lynn Foundation. Modeling conducted by Jeff Kiehl and Christine Shields. Data analysis and interpretation performed by William Rush. James Zachos and Jeff Kiehl conceived and supervised the project. WR wrote the manuscript with contributions from all co-authors.

Increased frequency of extreme precipitation events in the North Atlantic during the PETM: Observations and Theory

William D. Rush[1], Jeffrey T. Kiehl[1], Christine A. Shields[2], James C. Zachos[1]

[1]University of California, Santa Cruz, 1156 High Street, Santa Cruz, CA 95064, USA

[2]National Center for Atmospheric Research, PO Box 3000, Boulder, CO 80307, USA

Contact information: William D. Rush (wrush@ucsc.edu) *

Jeffrey T. Kiehl (jkiehl@ucsc.edu)

Christine A. Shields (shields@ucar.edu)

James C. Zachos (jzachos@ucsc.edu)

*Corresponding Author

Highlights:

- Newly obtained model output demonstrates significant hydrologic change in response to CO_2 forcing
- Modeled changes are largely in line with observed changes in regional sediment patterns
- Orbital configuration may have played a role in observed offsets in timing of sediment response relative to the CIE

Abstract

Climate model simulations of the PETM (Paleocene-Eocene Thermal Maximum) warming have mainly focused on replicating the global thermal response through greenhouse forcing, i.e. CO_2, at levels compatible with observations. Comparatively less effort has gone into assessing the skill of models to replicate the response of the hydrologic cycle to the warming, particularly on regional scales. Here we have assembled proxy records of regional precipitation, focusing on the Mid-Atlantic Coasts of North America (New Jersey) and Europe (Spain) to test the response of the hydrologic system to greenhouse gas forcing of the magnitude estimated for the PETM (i.e., 2x). Given evidence that the PETM initiated during a maximum in eccentricity, this includes the response under neutral and extreme orbital configurations. Modeled results show excellent agreement with observations in Northern Spain, with a significant increase in both mean annual and extreme precipitation resulting from increased CO_2 levels under a neutral orbit. The Mid Atlantic Coast simulations agree with observations showing increases in both overall and extreme precipitation as a result of CO_2 increases. In particular, the development of sustained atmospheric rivers might be significantly contributing to the extremes of the eastern Atlantic, whereas extratropical cyclones are likely contributing to the extremes in the western Atlantic. With an eccentric orbit that maximizes insolation during boreal summer, there is a suppression of extreme precipitation events in the eastern Atlantic and an amplification in the western Atlantic, which may account for

observations in the relative timing of the sedimentary response to the carbon isotope excursion associated with the PETM.

Increased frequency of extreme precipitation events in the North Atlantic during the PETM: Observations and Theory

William D. Rush[1], Jeffrey T. Kiehl[1], Christine A. Shields[2], James C. Zachos[1]

[1]University of California, Santa Cruz, 1156 High Street, Santa Cruz, CA 95064, USA

[2]National Center for Atmospheric Research, PO Box 3000, Boulder, CO 80307, USA

Contact information: William D. Rush (wrush@ucsc.edu) *

Jeffrey T. Kiehl (jkiehl@ucsc.edu)

Christine A. Shields (shields@ucar.edu)

James C. Zachos (jzachos@ucsc.edu)

*Corresponding Author

Keywords:

Paleocene-Eocene Thermal Maximum; model-data comparison; climate model; Mid-Atlantic; Pyrenees

1 Introduction

In response to greenhouse warming, the hydrological cycle is anticipated to intensify, as higher temperatures lead to a higher saturation vapor pressure, thus increasing the holding capacity of the atmosphere (Held and Soden, 2006). On a global scale the changes in evaporation will be manifested in large part by increased transport of vapor from the subtropics poleward. However, there is a good deal of variability between models (Carmichael et al., 2018) and within models both spatially and in how this intensification may manifest itself. Therefore, simple estimates of mean annual precipitation will not adequately capture the climatic response (Pfahl et al., 2017). This is due to the fact that climates are not influenced solely by the amount of precipitation that falls, but rather how it falls, e.g. whether the precipitation is evenly distributed throughout the year or is highly seasonal or episodic (e.g., cyclones, atmospheric rivers). This is particularly relevant to forecasting changes in the frequency and intensity of droughts and thus the impacts of global warming on terrestrial ecosystems and agriculture.

While models can provide excellent approximations of past or future climate states, there are inherent limitations due to the tradeoff between model complexity

and computational requirements. Processes that occur at scales smaller than the resolution of the model must be parameterized, e.g. cloud physics, and there is disagreement on the dynamics of these processes and how they are managed (Arakawa, 2004; Jakob, 2010; McFarlane, 2011; Christensen, 2020). As a consequence, the inability of models to simulate dynamics on finer spatial and temporal scales becomes increasingly problematic as the forcing (i.e., GHG) deviates further from the modern state. This is particularly so with the simulation of processes such as cyclones and atmospheric rivers that can influence the tail end distribution of precipitation extremes.

One potential strategy for assessing theory on intensification of the hydrologic cycle is to turn to Earth's past episodes of extreme greenhouse warming as represented in geologic archives (Carmichael et al., 2018). The Eocene epoch in particular is characterized by a series of rapid warming events referred to as "hyperthermals" (e.g., Littler et al., 2014). Each of these was likely driven by release of isotopically depleted C and rising greenhouse gas levels as evidenced by carbon isotope excursions and deep-sea carbon dissolution (i.e., ocean acidification). The largest carbon release occurred during the Paleocene-Eocene Thermal Maximum, or PETM, with estimates ranging from less than 4500 GtC to over 10,000 GtC (Zeebe et al., 2009, Gutjahr et al., 2017). As a consequence, mean global temperature rose over 5°C dramatically impacting regional climate and ecosystems (McInerney and Wing, 2011). While the exact mechanism that triggered the carbon release has been

disputed, it has been suggested that the PETM is the closest approximation to current anthropogenic global warming, although at a slower rate (Zeebe and Zachos, 2013).

The response of the global hydrologic cycle to the PETM warming was significant. Evidence for a mode shift in precipitation patterns or an "intensification" exists in locations around the world (Carmichael et al., 2018). On a global scale the planet appeared to become "wetter" consistent with an increase in the atmospheric holding capacity and transport of vapor with higher temperature. In detail, however, the mode of intensification varied regionally, with some regions appearing to become wetter, other regions dryer, or both in the sense of a change in the cycle of precipitation on seasonal or longer time scales. Some of the most notable changes have been observed in coastal P-E boundary sections located along the margins of the north Atlantic (John et al., 2008; Kopp et al., 2009; Schmitz and Pujalte, 2007). For example, the western Atlantic margin, the North Sea, and Bay of Biscay experienced an influx of kaolinite (Gibson et al., 2000; Kemp et al., 2016; Schmitz et al., 2001). This increase in kaolinite has also been noted at a number of other locations including central China, Tanzania, and Antarctica (Chen et al., 2016; Handley et al., 2012; Robert and Kennett, 1994). In most cases, it has been argued that this shift in clay mineral assemblage is not the result of enhanced chemical weathering further

leaching the clays, but rather an enhanced physical weathering eroding out previously deposited sediment (Gibson et al., 2000; Handley et al., 2012; John et al., 2012).

Previous modeling and observational studies of the PETM have addressed intensification of the hydrologic cycle on a global scale (Carmichael et al., 2018, Kiehl et al., 2018). Here, we assess regional intensification, focusing on the margins of the North Atlantic where observations exist for both coasts and thus have the potential to provide insight into the response of both large and small-scale processes. This includes processes such as atmospheric rivers and extratropical cyclones which play a role in the frequency of extreme precipitation events along eastern ocean boundaries and western ocean boundaries respectively (Laing and Evans, 2011; Ralph, 2019). Further detail on the changes to tropical cyclones and atmospheric rivers can be found in Kiehl et al., 2021 and Shields et al., 2021 respectively, which complement this study.

This study utilizes a 2 by 2 experimental design wherein the effects of CO_2 forcing and orbital forcing can be analyzed both independently and in conjunction in order to disentangle their effects. It has been argued that the onset of the PETM occurred near an eccentricity maximum (100 or 405-thousand-year; e.g., Zeebe and Lourens, 2019) suggesting some combination of orbital and greenhouse forcing on climate. Given the potential influence of orbital configuration on seasonal precipitation patterns and intensity in the Northern Hemisphere (e.g., the monsoons), analyzed simulations include an orbital configuration that maximizes insolation for

NH summers. To that end, we utilize the latest simulations of precipitation of the Community Atmosphere Model, Version 5.3, hereafter referred to as CAM5, as configured with late Paleocene and PETM boundary conditions, GHG forcing, and orbital configurations (Figure 1). We then analyze modeled hydrologic changes against compiled records from the North Atlantic margin and the Basque Basin to determine if the modeled response adequately captures the signal preserved in the sediment record. In particular, we assess the relative fit of the simulations of precipitation on scales relevant to the reconciliation of observations on a regional scale. While the observational constraints are limited in terms of constraining the exact nature of changes in precipitation, either amounts or seasonal distribution, we are able to combine multiple qualitative estimates of precipitation change in order to assess model fit.

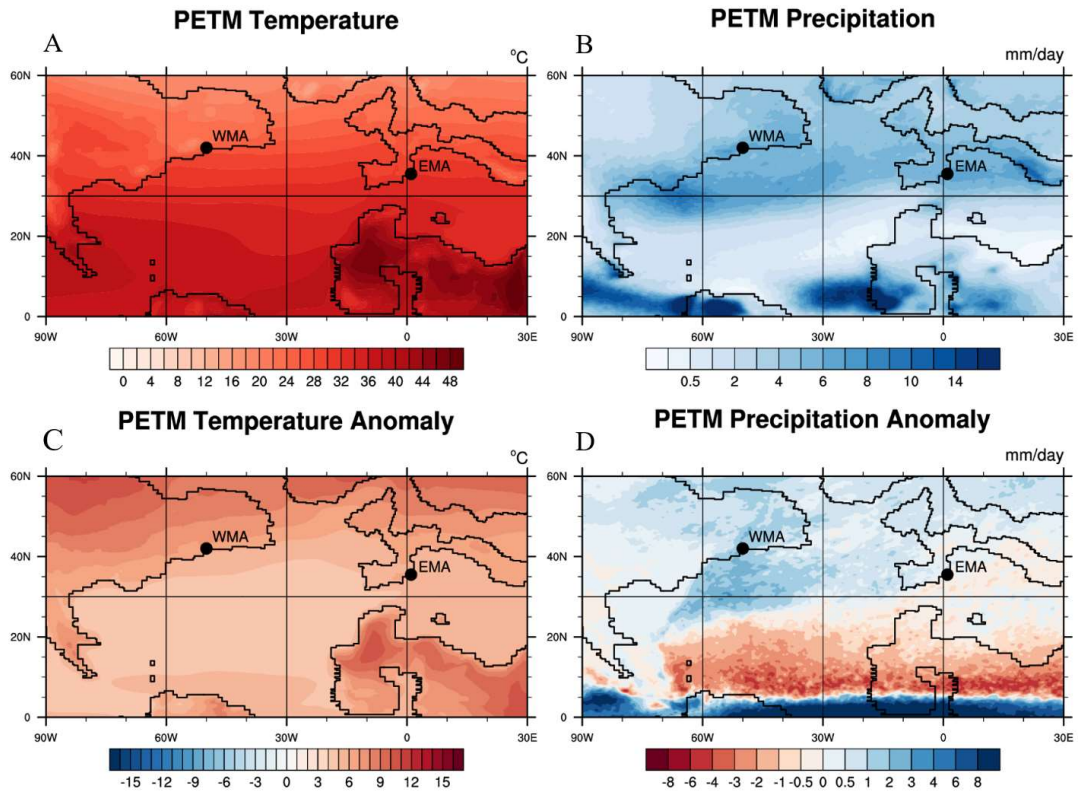

Figure 1: Paleoreconstruction of the of the North Atlantic during PETM overlain with CAM5 simulated PETM (pCO_2 =1590 ppmv) mean annual temperature (A), precipitation rate (B), and anomalies for each (C, D) relative to the late Paleocene (pCO_2 = 680 ppmv). Study locations marked by black dots. WMA = Western Mid Atlantic, EMA = Eastern Mid Atlantic.

2 Materials and methods

2.1 Depositional constraints on Atlantic coastal hydrology

The observational constraints for the western Mid-Atlantic (hereafter referred to as WMA) region come mainly from sites along from the New Jersey coastal plain

(Figure 1, Figure S1). The sediments obtained from these cores were deposited in the Salisbury Embayment on a shallow continental shelf on a passive margin. The full sedimentary succession ranges from the Cretaceous through the modern and is underlain by crystalline basement. The studied interval is comprised of the upper Paleocene Aquia Formation, a glauconitic, fine silty, clay-rich sandstone, overlain by lower Eocene Marlboro Clay, which is in turn overlain by the Nanjemoy formation, a glauconitic, fine, silty, clay-rich sandstone similar to the Aquia (Self-Trail et al., 2017). All records of sedimentation and climate from the New Jersey shelf sequences unequivocally support a significant mode shift in the regional hydrologic cycle during the PETM. Sedimentation rates increased several-fold despite rising sea level as the flux of siliciclastics, including kaolinite, to the coastal ocean increased (Gibson et al., 2000; John et al., 2008; Stassen et al., 2012). Moreover, dinoflagellate assemblages shifted from open marine toward more low-salinity tolerant species and bacterial magnetofossils akin to the distribution observed within modern-day sediments off the coast of the Amazon river increased in abundance and diversity (Sluijs and Brinkuis, 2009; Kopp et al., 2009; Lippert and Zachos, 2007). Collectively, the changes in depositional rates, lithology, and fossil assemblages are consistent with increased runoff and erosion on a mean annual and/or seasonal basis. Similar observations have been reported for P-E sections approximately 75 miles to the southwest in Maryland (Lyons et al., 2019).

The primary observational constraints for the eastern Mid-Atlantic (hereafter referred to as EMA) considered in this study come from units deposited in the Basque

Basin of Northern Spain. These basins contain PETM sections deposited in terrestrial and shallow and deep marine settings (Figure 1, Figure S1). The terrestrial sections are comprised of paleosols and floodplain deposits deposited in the late Paleocene that transition to the large-clast (up to 65 cm) Claret Conglomerate during the CIE before transitioning back to deposits similar to the late-Paleocene (Schmitz and Pujalte, 2007). Computations of channel dimensions suggest a substantial rise in discharge rates during the PETM (increasing from 31 ± 4.3 m^3s^{-1} to 253 ± 102 m^3s^{-1}) (Chen et al., 2018). The deep marine sections are comprised primarily of hemipelagic limestones and marlstones transitioning into low-calcareous kaolinite-rich clays and silty clays during the CIE, returning to hemipelagic limestones and marlstones after the recovery (Pujalte et al., 2015). During the peak PETM, sedimentation rates in the distal, deep-water portion of the basin are estimated to have increased 4-fold (Dunkley Jones et al., 2018). Although debated, several sites appear to show a "temporal lag" between the onset of the PETM and the changes in sedimentation (Duller et al., 2019).

2.2 PETM climate simulations

A series of experiments simulating the PETM warming have been conducted (Kiehl et al., in prep; Shields et al., in prep) utilizing the high resolution (0.25°) CAM5, Version 5.3, with fixed sea surface temperatures and finite volume dynamical (FV) core, with 30 levels in the vertical for the atmosphere component (Neale et al., 2010; Park et al., 2014). The land component is the Community Land Model, Version

4 (CLM4) (Lawrence et al., 2011), also at 0.25° resolution, with the river transport model (RTM) at 1° resolution. Organic aerosol emissions were produced by running MEGAN (Model of Emissions of Gases and Aerosols) approximated from PETM biomes using DeepMIP protocols (Guenther et al., 2012; Lunt et al., 2017). The boundary conditions and sea surface temperatures from this model were obtained from a fully coupled LP and PETM FV 2° CESM1.2.2 (Community Earth System Model, Version 1.2) with output taken at a monthly temporal resolution over 1800 years.

Output was obtained from CAM5 at 6 hourly, daily, and monthly temporal resolution for over 20 years. The model was run with late Paleocene CO_2 values of 680 ppmv (hereafter referred to as LP) and PETM CO_2 values of 1590 ppmv (hereafter referred to as PETM). Methane was held at 16 ppmv in all runs. Additionally, in order to test the impact of orbital forcing, the model was run with both a neutral orbit and a configuration that maximized solar insolation over the northern hemisphere (i.e. High eccentricity, perihelion NH summers), hereafter referred to as OrbMax. Solar forcing was calculated based on a solar constant of 1355 Wm^{-2} consistent with Kiehl et al. (2018). The four runs are therefore referred to as LP, PETM, LP OrbMax, PETM OrbMax (Table 1). Paleocoordinates for each location were set over a 2° by 2° area and were taken from the DeepMIP protocols (Lunt et al., 2017). EMA was set to 34.5°-36.5°N, 0°-2°E. WMA was set to 41°-

43°N, 49°-51°W. In order to account for the time required for the model to reach equilibration, data was trimmed to the final 15 years of the 20-year model run.

Table 1: Explanation of model parameter abbreviations

	Neutral Orbit	Maximized NH Summers
Low CO_2 (680 ppmv)	LP	LP OrbMax
High CO_2 (1590 ppmv)	PETM	PETM OrbMax

The parameters of interest include median and 1st and 3rd quartile monthly precipitation and runoff to track both annual and seasonal variation, and exceedance frequency to track storm intensity and to track changes in frequency of storm events. Exceedance frequency is calculated as $\boldsymbol{P = m \div (n + 1)}$, wherein $\boldsymbol{P}$ is the exceedance frequency, $\boldsymbol{m}$ is the rank of a given event, and $\boldsymbol{n}$ is the total number of events.

3 Results

PETM simulations show increases in temperatures with the largest increases occurring at high latitudes, and changes in mean annual precipitation consistent with the "wet gets wetter, dry gets drier" trend noted in Held and Soden (2006), with increases to precipitation occurring in the tropics and high latitudes and decreases in the subtropics (Figure 1). Applying the OrbMax configuration results in enhanced seasonality of temperatures in the northern hemisphere, i.e. hotter summers and colder winters, with a more varied hydrologic response, demonstrating latitudinal

shifts in precipitation patterns and changes in intensity of seasonal precipitation (Figures S3-S10).

Precipitation data from the high-resolution 0.25° model (CAM5) for all simulations was extracted and evaluated for 2° by 2° regions in the Mid-Atlantic and Pyrenees. The extracted output includes annual precipitation and runoff, exceedance frequency of precipitation events and runoff, and median and quartile precipitation and runoff for each month.

For the WMA, mean annual precipitation increases by 14.3% from 1885 mm/year in the LP run to 2155 mm/year in the PETM run; however, this is highly seasonal, with the largest overall increases occurring during September through December when comparing the LP and PETM (Figure 2). There is a significant increase in the exceedance frequency of individual storm events and runoff events, and intensity of individual storm events experiences its greatest change in May through October (Figures 2, 3).

A New Jersey Median Monthly Precipitation Rate

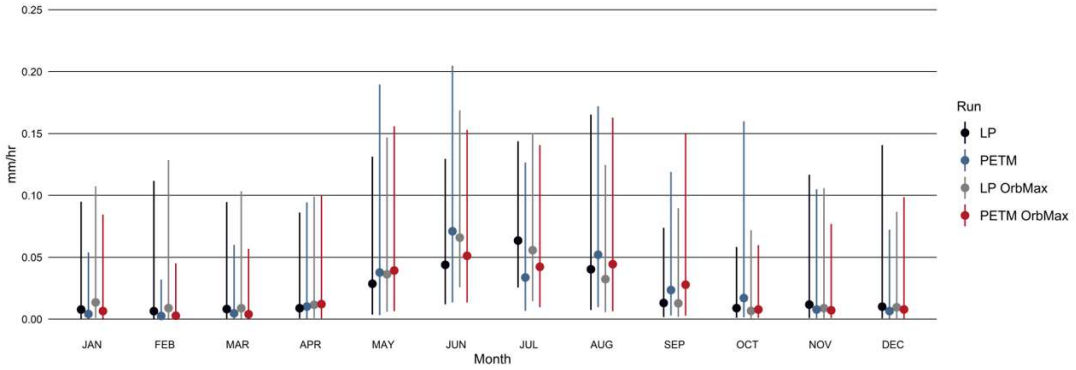

B New Jersey Median Monthly Runoff Rate

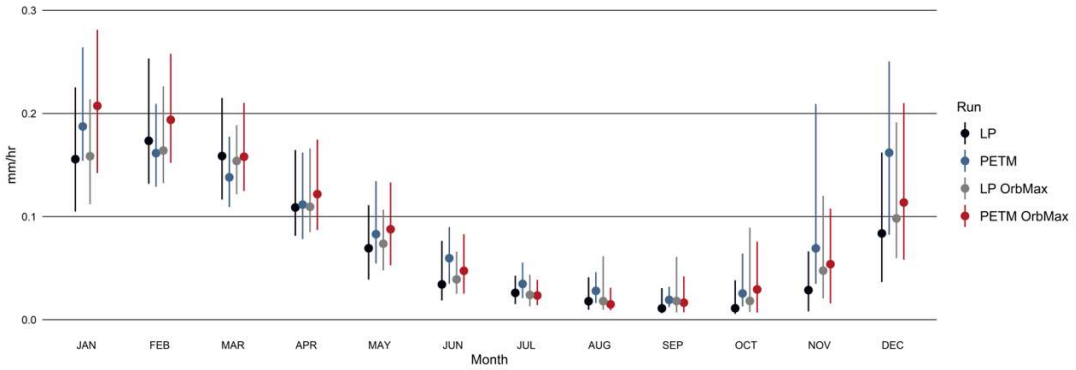

C Pyrenees Median Monthly Precipitation Rate

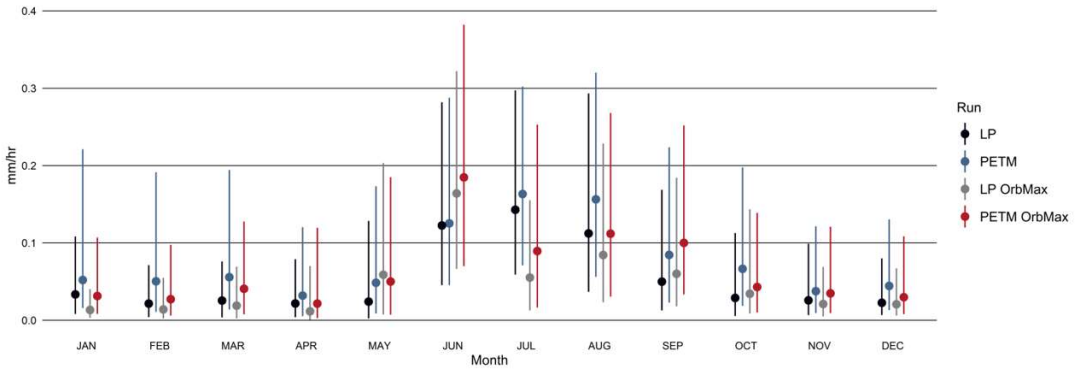

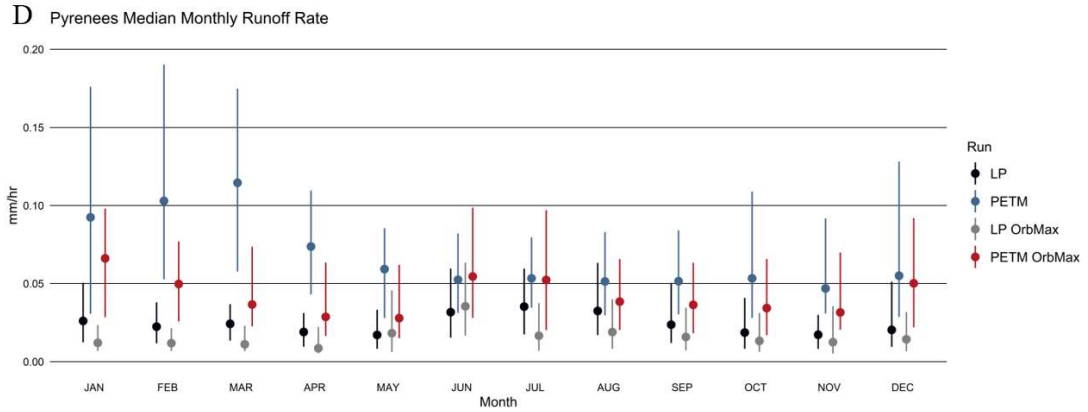

Figure 2: Comparative modeled median precipitation (A, C) and runoff (B, D) rates in the Mid-Atlantic region (A, B) and Northern Spain (C, D) for late Paleocene and PETM CO_2 levels with and without maximizing insolation in the northern hemisphere during boreal summer. Error bars represent 1st and 3rd quartile precipitation rates. For all model runs, n=21,900. Note increased seasonality of extreme precipitation in New Jersey during the PETM evidenced by increase in 3rd quartile in summer and decrease in winter. OrbMax runs show similar trends to their neutral orbit counterparts. For Northern Spain, note increase in intensity of winter precipitation resulting from increased CO_2 levels, but a reduction in intensity (and runoff) in the OrbMax configuration.

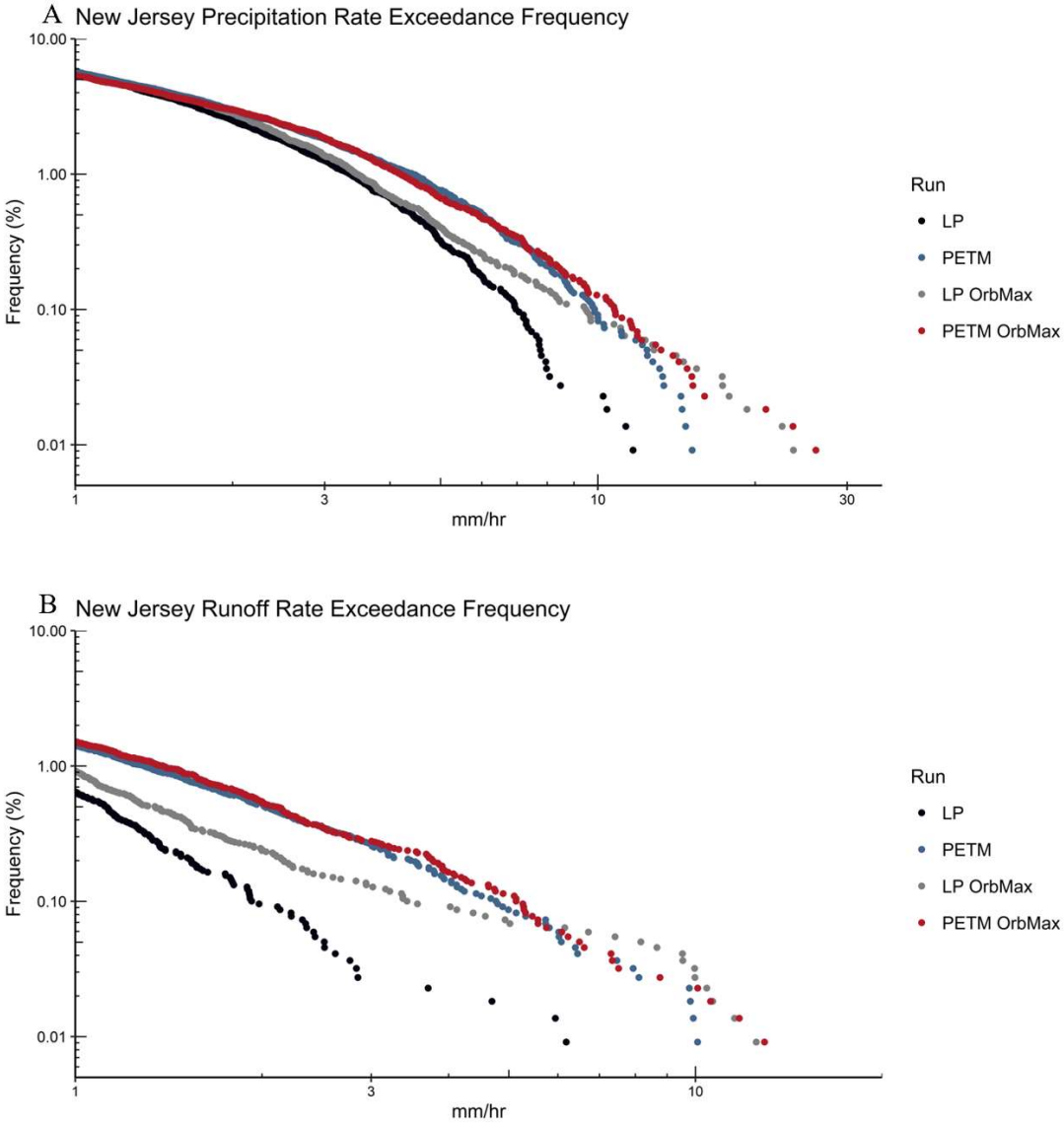
A New Jersey Precipitation Rate Exceedance Frequency
10.00
1.00
0.10
0.01
Frequency (%)
1
3
10
30
mm/hr
Run
LP
PETM
LP OrbMax
PETM OrbMax
B New Jersey Runoff Rate Exceedance Frequency
10.00
1.00
0.10
0.01
Frequency (%)
1
3
10
mm/hr
Run
LP
PETM
LP OrbMax
PETM OrbMax

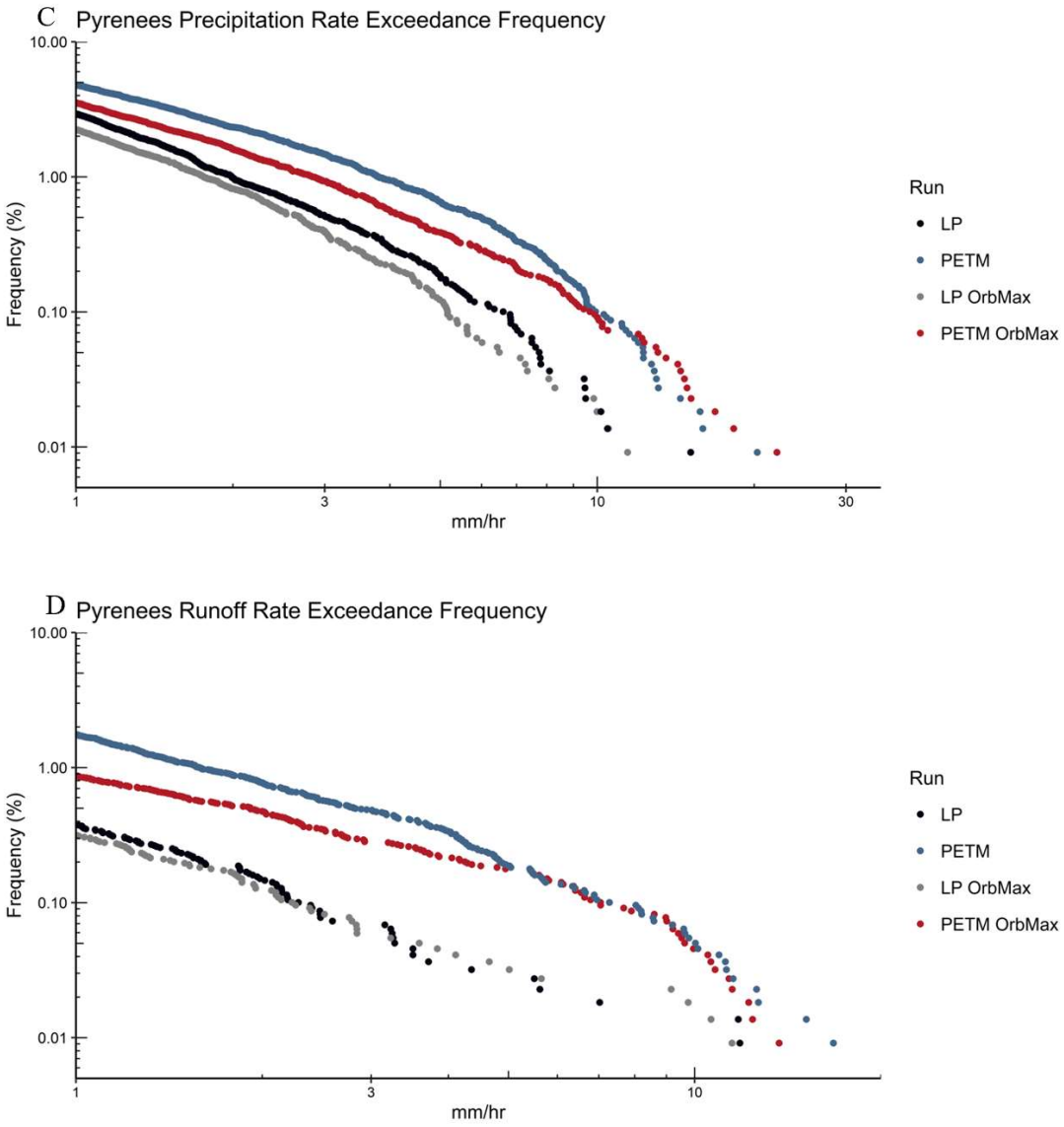

Figure 3: Modeled exceedance frequency of precipitation (A, C) and runoff (B, D) events at late Paleocene and PETM CO_2 levels with and without maximizing solar insolation over the Northern hemisphere for the Mid-Atlantic (A, B) and Northern Spain (C, D). For all model runs, n=21,900. For precipitation in New Jersey, note the increase in frequency and intensity of storm events in both CO_2 and orbitally forced

runs. For precipitation in the Pyrenees, note increases related to CO_2 forcing, and decreases related to orbital forcing.

Applying the OrbMax configuration to the LP run results in mean annual precipitation increases of 7.3% from 1885 to 2024 mm/year. Average monthly total precipitation is higher for every month, but the greatest differences are in July and August, likely due to the higher insolation during summer months. In terms of the intensity of individual events, there is little change in the 3rd quartile between the LP and LP OrbMax configurations, but the exceedance frequency demonstrates dramatic increases to both runoff and precipitation rates (Figures 2, 3).

For the PETM run, applying the OrbMax configuration resulted in changes to overall precipitation intermediate to those observed from either CO_2 or changing the orbital configuration alone, with an increase of 11.5% to 2101 mm/year compared to the LP run. The exceedance frequency showed an increase in storm intensity, with increases largely occurring in summer months, similar to CO_2 forcing alone (Figures 2,3).

Modeled runoff for the WMA region shows similar trends to precipitation when comparing the model runs; however, there is a shift in the seasonal timing, perhaps due to seasonal variations in evapotranspiration owing to increased insolation and elevated temperatures in summer months or groundwater recharge within the land component of the model (Figures 2, 3). The PETM run has the highest rate of runoff, with an average of 1311 mm/year, a 36.8% increase over the 958 mm/year during the

LP run, with the average monthly totals increasing in every month except February and March, and the greatest increases occurring in October through January. In contrast to precipitation, the greatest variability also occurs in the winter months.

Hydrologic shifts in the EMA are even more pronounced, with an increase of 55.2% in mean annual precipitation from 1531 mm/year in the LP run to 2376 mm/year in the PETM run. On a monthly basis, the increase in precipitation is spread throughout the year, with the largest changes occurring in January, February, and March. Much of this increase appears to be in the form of more extreme precipitation during these months as evidenced by the shift in the 3rd quartile during this time (Figures 2, 3).

However, unlike the WMA, relative to the neutral orbit LP at OrbMax resulted in a net decrease of mean annual precipitation of 14.5% from 1531 mm/year to 1310 mm/year. Moreover, the monthly averages of LP OrbMax show a trend of increasing seasonality, with increased precipitation in summer during the LP OrbMax run and decreased precipitation in winter, the exception being July, which shows a drop in the mean total from 184 mm in the LP run to 86 mm in the LP OrbMax run.

The PETM OrbMax run in the EMA showed a net increase in precipitation of 24.7% to 1910 mm/year, significantly lower than the PETM run. Additionally, the exceedance frequency exhibits an overall decrease in the intensity of precipitation, trailed only by the LP OrbMax run. There were marginal increases in the intensity of

winter precipitation evidenced by the 3rd quartile, and variable increases or decreases in summer precipitation compared to the LP run.

Runoff in the EMA region demonstrates even greater shifts, with the PETM having the highest rates at 1230 mm/year, an increase of 179% over the 439 mm/year from the LP run. Similarly, the OrbMax configuration resulted in a decrease in total runoff, with 346 mm/year in the LP OrbMax run and 802 mm/year in the PETM OrbMax run.

4 Discussion

In terms of a hydrologic regime shift, the observed changes in the character of sedimentation during the PETM at the two locations considered here could be explained by the following: a change in seasonality with enhanced wet-dry cycles leading to denudation of the landscape from the dry season and the erosion of newly barren soil during the wet season (Schmitz and Pujalte, 2007; Molnar et al., 2001), increasing the frequency and intensity of storm events (Molnar et al., 2001; Eden and Page, 1998; Rossi et al., 2016) or by simply increasing the overall precipitation (MAP) (Langbein and Schumm, 1958). These impacts are by no means exclusive from one another and may work in conjunction. For example, Anderson (1954) found levels of sediment discharge to be correlated with both fluvial discharge and the "peakedness" of the fluvial discharge, i.e. the variation between periods of low flow and periods of high flow. This relationship is somewhat complicated as these increases in precipitation driving erosion are counterbalanced by increased vegetation

cover stabilizing soils, i.e. going from an arid climate to one with moderate rainfall can increase sedimentation rates, but further increases can stabilize the landscape through increased vegetation (Langbein and Schumm, 1958; Nearing et al., 2005).

We first consider the simulated changes in MAP of the two mid-Atlantic coasts in response to GH forcing under neutral and maximum boreal summer insolation orbits. Both studied locations experience increases in overall MAP in response to PETM greenhouse forcing. These increases are damped slightly under the OrbMax configuration in the WMA, and more significantly in the EMA. Overall, the changes in MAP (<15%) taken on their own are inadequate to explain the observations of increased sedimentation rates in the WMA regardless of orbital configuration. These changes are greater in the EMA (>50%), however, this increase is highly seasonal, which may have influenced erosion rates (Anderson, 1954; Molnar et al., 2001) (Figure 2). In both instances, the late Paleocene background precipitation rate of 2273 mm/yr in the WMA and 1531 mm/yr in the EMA are beyond the 355 mm/yr suggested as the upper limit by Langbein and Schumm (1958) in which increases in MAP would influence sediment yields.

We next consider the intra-annual extremes of precipitation. Previous studies have found this to have a significant impact on erosion rates, more so than changes in rainfall amount alone (Nearing et al., 2005). The simulated increase in greenhouse gas forcing does significantly increase the frequency and intensity of storm events on both North Atlantic coasts as evidenced by the changes in the exceedance frequency

(Figure 3). However, the intensity of extreme precipitation varies at each location depending on orbit. The CO_2 forcing increases the frequency and intensity of extreme precipitation events on both coasts, but maximizing solar insolation during boreal summer resulted in differing signals. The EMA experienced a drop in frequency in the moderate events (<5 mm/hr) in response to the OrbMax forcing, while the extreme events (>5 mm/hr) were comparable to, and often exceeded the neutral orbit runs in both frequency and intensity. The WMA frequency of extreme precipitation was largely the same between the neutral orbit and OrbMax runs for moderate events regardless of CO_2 forcing, but the OrbMax runs experienced an increase in the frequency of extreme events, particularly for the LP CO_2 levels (Figure 3).

The drop in moderate scale events in the EMA under the OrbMax configuration appears to be due at least in part to the seasonality of extreme precipitation events. While extreme precipitation in the Mid-Atlantic occurs primarily during boreal summer months, the greatest change to extreme precipitation in the Pyrenees occurred during boreal winter months (Figure 2). This damped response under OrbMax can be attributed to the reduction in energy in the northern hemisphere during winter months as insolation is concentrated in summer months (i.e., perihelion). In this regard, future characterization of extreme precipitation events during the PETM should focus on extending the duration of the model runs to analyze

shifts in more infrequent, stronger storms, e.g. 100-year storms, as well as testing the effects of maximizing insolation during boreal winter, i.e. aphelion.

In the WMA, both the PETM run and the PETM OrbMax run demonstrate significantly increased precipitation during the summer months alongside slightly drier conditions in winter months compared to the neutral orbit late Paleocene run. This has the potential to shift the hydrodynamics of regional catchments to a more erosive state (Schmitz and Pujalte, 2007; Molnar et al., 2001). Combined with the increased storm activity (Figures 2, 3 and S2) and increases in mean annual runoff on 36.8% compared to LP run, this supports the observations of increases in regional sedimentation rates of 2.8 to 220-fold late Paleocene values (Stassen et al., 2012), the sudden abundance of more low-salinity tolerant dinoflagellate cysts (Sluijs and Brinkhuis, 2009), and the appearance of bacterial magnetofossils associated with high discharge environments (Kopp et al., 2009).

In the EMA, the modeled changes are broadly in agreement with observations. The deposition of the Claret Conglomerate with clasts of up to 65 cm alongside a flux of kaolinite to the Basque Basin indicate a strengthening of the hydrologic cycle (Schmitz and Pujalte, 2007; Schmitz et al., 2001). Estimates of streamflow in the region based on channel dimensions estimate an increase in discharge of 1.35 to 14.9-fold (Chen et al., 2018). This is consistent with the modeled predictions of an increase in mean annual runoff of 2.79-fold from the PETM run compared to the LP run. The modeled changes in precipitation can be linked to an increase in the intensity of

atmospheric river related precipitation (Shields et al., 2021). Although the timing of sediment changes relative to the onset of the PETM in this region has been controversial on the basis of defining lithologic units (Pujalte and Schmitz, 2014), if the interpretations of Duller et al., 2019 are correct, the observed delays (~ 16 ±7.5 k.y.) may be related to orbital variation, as the OrbMax configuration results in a suppression of precipitation and runoff, both in the late Paleocene and the PETM (with precession, the delay would be ~10 k.y.). If these interpretations are not correct, it is possible that the reduced hydrologic activity noted in the OrbMax configuration of the model may have resulted in a period of nondeposition or was eroded by later, more intense hydrologic activity.

Delving into the model beyond the simulated changes in precipitation, the dynamical forcing seems to fit with these interpretations. Eddy kinetic energy, defined as $(\boldsymbol{u'^2 + v'^2})/\mathbf{2}$, wherein $\boldsymbol{u'}$ is the zonal component of the difference between the instantaneous and average wind velocity ($\boldsymbol{u' = u - \bar{u}}$), and $\boldsymbol{v'}$ is the meridional component, can be used as a means of analyzing changes in storm tracks (O'Gorman, 2010). For boreal winter, there is a reduction in eddy kinetic energy in the Mid-Atlantic region in response to both higher CO_2 and NH insolation (Figure S2). These observations are in line with the reduction in precipitation. The Iberian

Peninsula experiences drops in eddy kinetic energy in the OrbMax runs, but increases in response to CO_2, again in line with precipitation changes.

Changes to eddy kinetic energy in boreal summer are much more complicated, with very different signals between the 250 mbar and 700 mbar pressure levels, indicating much of the precipitation for both locations during this season is not necessarily linked to large scale jets or the jet-driven storm tracks. Focusing on the Mid-Atlantic, during this season, there is a significant increase in convective precipitation during the PETM runs compared to the LP runs, while non-convective, large-scale precipitation remains relatively constant, indicating these changes are likely due to locally generated thunderstorms. However, holding CO_2 constant and maximizing summer insolation via orbit results in greater changes to large-scale precipitation than convective, suggesting precipitation is related to surface lows or frontal boundaries, but are are just surface disturbances clearly not connected to the steering flow.

In Northern Spain, the GHG forcing results in increases in both convective and large-scale precipitation particularly during winter months, the most significant being increases in large scale storm tracks, likely driven by an increase in

atmospheric river activity, which are most active in the winter months in this region. In the OrbMax configuration, however, both are reduced.

5 Conclusions

Model predictions demonstrate both the Mid-Atlantic and Northern Spain experienced significant changes in hydroclimate as a result of higher CO_2 during the PETM. The most prominent changes are increases in the frequency and intensity of precipitation events and the seasonal timing of these events, which are likely the driver of the observed changes in sedimentation. These modeled changes are broadly in agreement with observations in each region. However, compounding the effects of CO_2 forcing with changes in orbit results in divergent signals, with the Mid-Atlantic region staying largely in line with the changes from CO_2 alone, and the Pyrenees seeing a suppression of the effects of CO_2 forcing. These varying responses may contribute to the observed variation in the timing of hydrologic changes relative to the carbon isotope excursion on either side of the Atlantic. On balance, the agreement between models and observations of the PETM increases confidence in general theory of intensification of the hydrologic cycle in response to significant increases in

greenhouse gas levels in Earth's past and in the not so distant future. This includes the increased frequency of extreme precipitation events.

Acknowledgments and data

Mathew Rothstein and Mark Snyder contributed to model construct. Funding for this project was provided by a Heising-Simons Foundation Grant to JTK, an NSF grant (OCE-1415958) to JCZ and the Ida Benson Lynn Foundation. Modeling conducted by Jeff Kiehl and Christine Shields. Data analysis and interpretation performed by William Rush. James Zachos and Jeff Kiehl conceived and supervised the project. WR wrote the manuscript with contributions from all co-authors.

Model output was generated using the CAM5.3 FV (finite volume) dynamical core high-resolution (0.25 degree version) model run for 20 years (Neale et al., 2010; Park et al., 2014), with CLM4.0 for the land component (Lawrence et al., 2011), and MEGAN for the aerosol emissions (Guenther et al., 2012). Sea surface temperatures for CAM were fixed using CESM1.2.2, which was run for 1800 years and fully coupled for boundary conditions, and is publicly available at http://www2.cesm.ucar.edu/models/cesm1.2/. Boundary data including topography, bathymetry, and land use were obtained from the DeepMIP repository (Lunt et al., 2017). Total model output for these model runs is stored on the NCAR computing cluster, and may be accessed by contacting Christine Shields (shields@ucar.edu). Model output used in generation of figures is available for download at https://datadryad.org/stash/dataset/doi:10.7291/D1FQ18.

Comparative Climatic Changes Between the PETM and ETM2 in the Salisbury Embayment

William Rush[1], Jean Self-Trail[2], Yang Zhang[3], Appy Sluijs[4], Henk Brinkhuis[4,5], James Zachos[1], James G Ogg[6,7,8], Marci Robinson[2]

[1]Department of Earth and Planetary Sciences, University of California Santa Cruz, 1156 High Street, Santa Cruz, CA 95064, USA

[2]Florence Bascom Geoscience Center, U.S. Geological Survey, Reston, Virginia, USA

[3]Faculty of Geosciences, University of Bremen, Bremen, Germany

[4]Department of Earth Sciences, Faculty of Geosciences, Utrecht University. Princetonlaan 8a, 3584 CB Utrecht, The Netherlands

[5]Dept of Ocean Systems research, NIOZ Royal Netherlands Institute of Sea Research, PO Box 59, 1790 AB Den Burg, Texel, The Netherlands

[6]Department of Earth, Atmospheric and Planetary Sciences, Purdue University, 550 Stadium Mall Drive, West Lafayette, IN 47907-2051, USA

[7]State Key Laboratory of Oil and Gas Reservoir Geology and Exploitation, Chengdu University of Technology, 610059 Chengdu, Sichuan, China

[8]International Union of Geological Sciences, Deep-time Digital Earth Research Center of Excellence (Suzhou), 1699 Zu Chongzhi South Road, Kunshan (Jiangsu), China

Correspondence to: William Rush (wrush@ucsc.edu)

Abstract. Eocene transient global warming events (hyperthermals) can provide insight into our future, warmer world. While much research has focused on the Paleocene-Eocene Thermal Maximum, hyperthermals of smaller magnitude can be used to characterize climatic responses over different degrees of forcing. This study has identified two events, Eocene Thermal Maximum 2 (ETM2 and H2) for the first time in a shallow marine setting along the US Atlantic margin in the Salisbury Embayment of Maryland, based on magnetostratigraphy, calcareous nannofossil biostratigraphy, and recognition of negative stable carbon isotope excursions (CIEs) in biogenic calcite. We assess local environmental change utilizing clay mineralogy, marine palynology, $\delta^{18}O$ of biogenic calcite, and biomarker paleothermometry (TEX_{86}). Temperature proxies show broad agreement between surface water and bottom water temperature changes. However, the timing of warming does not correspond to the CIE as expected, and the highest values are observed at H2, suggesting factors other than CO2 forcing influenced temperature changes in the region. The ETM2 interval exhibits a shift in clay mineralogy from smectite-dominated facies to illite-rich facies, suggesting hydroclimatic changes but with a rather damped weathering response relative to that of the PETM. Dinoflagellate cyst assemblages show large fluctuations throughout the studied section, none of which seem systematically related to ETM2, contrary to the tight correspondence between climate change and assemblages across the PETM, regionally and globally, and ETM2 in the Arctic Ocean. They do indicate very warm and (seasonally) stratified conditions, likely salinity-driven, across H2. The absence of evidence for strong

perturbations in hydrology and nutrient supply, in combination with relatively muted sedimentological and chemical change, suggests that ETM2 and H2 drove insufficient climatic perturbation to drive strong environmental change in mid-latitude regions.

1 Introduction

The early Eocene is punctuated by a series of transient phases of carbon input and global warming, termed hyperthermals (e.g., Cramer et al., 2003; Littler et al., 2014). The well-studied Paleocene-Eocene Thermal Maximum (PETM) may represent the closest approximations to modern day warming in the geologic record (Zachos et al., 2008). However, debate exists as to the origins of this event with respect to its timing and the source of carbon (Zeebe & Lourens, 2019; Zachos et al., 2010; Reynolds et al., 2017; Dickens et al., 1997; Frieling et al., 2019). Deep ocean records contain gaps in carbonate-based proxy records due to the rapid ocean acidification that accompanied it (Zachos et al., 2005). Along continental margins, the PETM is marked by strong hydrological, sedimentological and biotic perturbations, for example in the Salisbury Embayment, located within the Mid-Atlantic Coastal Plain of the United States (Kopp et al., 2009; Sluijs & Brinkhuis, 2009; Stassen et al., 2012b; Self-Trail et al., 2012; Self-Trail et al., 2017; Rush et al., 2021). However, with the variety of projected pathways predicted by the IPCC AR6 (Masson-Delmotte et al., 2021), study of how smaller perturbations to the carbon cycle affect regional climates is critical. Eocene Thermal Maximum 2 (ETM2) occurred ~2 million years after the PETM and appears to be an event of roughly one third to half the magnitude of the PETM regarding carbon input and warming (Lourens et al., 2005; Sluijs et al.,

2009; Stap et al., 2010; Dunkley Jones et al., 2013; Gutjahr et al., 2017; Harper et al., 2020). Therefore, ETM2 can provide insight into the climatic impacts of a smaller carbon forcing when compared to the PETM from geographically similar sites, and hence sensitivity to greenhouse forcing. In this study, we identify ETM2 and the 100 kyr younger event H2 in the Salisbury Embayment and develop the first records of the regional climatic/environmental impacts.

One critical feature of the climatic response to greenhouse forcing is intensification of the hydrologic cycle (e.g., Carmichael et al., 2017). Indeed, studies of the PETM show a pronounced mode shift with evidence of increased frequency of precipitation extremes leading to high energy fluvial activity. This includes mid-Atlantic margin settings where coastal archives record increased seasonal sediment fluxes indicative of enhanced erosion during the PETM (John et al., 2008; Self-Trail et al., 2017; Stassen et al., 2012b; Rush et al. 2021). Similar signals have been found in many regions across various hyperthermals, including the Pyrenees, the margins of the Tethys, and the North Sea Basin (Schmitz & Pujalte, 2007; Sluijs et al., 2014; Jiang et al., 2021; Sluijs et al., 2007; Jin et al., 2022). These changes in extreme precipitation patterns are consistent with projections for future change (Pfahl et al., 2017; Swain et al., 2018). Therefore, studying the impacts of hydroclimatic changes in response to differing degrees of carbon forcings can inform as to the linearity of these responses, "tipping point" thresholds, and background variability of the hydrosphere.

Given the extensive evidence of a mode shift in coastal mid-Atlantic hydroclimate during the PETM, we initiated a regional search for ETM2. We here identify ETM2

and H2 in the Knapps Narrows core based on biostratigraphic, paleomagnetic, and chemostratigraphic data. We present proxy records of the regional climatic response, including foraminiferal $\delta^{18}O$ and TEX_{86} based temperature reconstructions, clay mineralogy, and dinoflagellate cyst assemblages.

2 Materials and Methods

2.1 Material

The Knapps Narrows core was drilled at 38.72129, -76.33162 on the Eastern Shore of Maryland. The cored target interval lies between 84-102 meters through the Nanjemoy Formation. From the bottom of the section to 88.4 meters, lithology is dominated by very coarse to fine, poorly sorted, angular to subrounded sand comprised of ~50% glauconite, ~30% quartz, and <5% muddy matrix. Between 88.4 meters to the top of the section, the core largely consists of very coarse to medium, subrounded to angular clayey sand with poorly sorted glauconite (~40%) and quartz (~10%) in a muddy matrix (20%). Sand coarsens downsection and clay content increases. The core is heavily bioturbated throughout. The core contains an expanded interval over NP11, which contains ETM2, and compared to the surrounding cores, the Marlboro Clay deposited during the PETM is entirely absent. This disconformity and resultant paleobathymetry likely contributed to the enhanced sedimentation rates and expanded section recorded in the core (Supplemental Figure 3). Initial core description noted much coarser grain-sizes compared to the Nanjemoy in surrounding cores, further supporting the interpretation of rapid infill during this time period. All raw data are included in the supplement.

2.2 Methods

2.2.1 Nannofossil Biostratigraphy

Nannofossil zonation was established and core descriptions were logged in the field and at the Florence Bascom Geoscience Center (USGS). Forty-two samples for calcareous nannofossil analysis were taken from the center of freshly broken core in order to avoid contamination from drilling fluid. Smear slides for calcareous nannofossil analysis were prepared using the standard technique of Bown and Young (1998) combined with the double slurry technique of Blair and Watkins (2009) and mounted using Norland Optical Adhesive 61. Slides were examined under cross-polarized light using a Zeiss Axioplan 2 light microscope (LM) at 1250x magnification. Biostratigraphic zones assigned to each species were based on the NP zonation of Martini (1971) and supplemented by the biohorizons of Agnini et al. (2014). Smear slides are housed in the U.S. Geological Survey calcareous nannofossil laboratory in Reston, VA.

2.2.2 Paleomagnetism

Paleomagnetic data was generated at the Department of Earth, Atmospheric and Planetary Sciences at Purdue University. A total of ~100 minicores were collected from the Knapps Narrows core (40–110 m). The sampling spacing was roughly from 0.2 to 1.5 m, and was guided by preliminary biostratigraphy. For example, a sampling gap of ~8 m happened in the lower Nanjemoy Formation because this interval was expected to fall in the reversed polarity, i.e., upper C24r in nannofossil Zone NP10.

Given that sediments are largely semi-consolidated, a non-magnetic plastic tube was inserted, and then the sediment plug was pushed out into aluminum foil pieces and tightly wrapped. Occasionally, paleomagnetic samples were taken by pushing non-magnetic cubes directly into the center of the core halves so that alternate field demagnetization could be used.

Stepwise thermal demagnetization in an ASC Model TD 48-SC thermal demagnetizer was applied to a majority of the samples followed by measurement on a three axis 2G Enterprises 755 superconducting rock magnetometer. Heating involved at least 7 treatments, at ~25 °C/50 °C steps from 100 °C to 350 °C for the weak samples and up to 575-600 °C for stronger ones. Thermal demagnetization generally ceased when the remanent magnetization displayed either anomalous surges in magnetization, was too weak for magnetometer precision, or exhibited irregular magnetic directions/intensities for two or three consecutive steps. The choice of a thermal rather than an AF-demagnetization procedure was due to potential existence of high-coercivity magnetic minerals (e.g., goethite).

The interpreted polarity and characteristic directions of the samples were given a quality rating of 'N(R)', 'NP(RP)', 'NPP(RPP)', 'N?(R?)' or 'INT' according to a semi-subjective judgment of the behavior of the magnetic vectors during the stepwise demagnetization. The 'N/R' ratings were generally assigned to those samples that attained a (semi-)stable endpoint direction (Characteristic remanent magnetization, or ChRM) during progressive demagnetization. However, only a small subset of our samples displayed this ideal resolution of primary magnetization. We applied a 'P'

tag of ‘RP’ or ‘NP’ when the residual magnetization vector was considered close to attaining an endpoint before losing its residual magnetization or experiencing a surge. The ‘PP’ tag was applied to samples that had a distinct trend toward the polarity hemisphere to be considered indicative of the underlying polarity but were considered to be too far from attaining an endpoint before dying to be used in statistics for computing a mean direction. The ‘?’ qualifier was used to denote possible trends toward an underlying polarity, and ‘INT’ is either entirely uncertain or displayed an endpoint that was intermediate between the ‘N’ and ‘R’ poles.

Polarity zones were assigned to stratigraphic clusters of ChRM vectors rated as N-NP-NPP or R-RP-RPP. Uncertain intervals were assigned to clusters of N?-INT-R? and to significant gaps in sampling coverage. Summary plots of the lithology of the Knapps Narrows with the interpreted polarity patterns (Supplemental Figure 1) were generated with the public TSCreator visualization software (https://timescalecreator.org).

Samples from rotary cores have no control on their declination orientation. The overprint components from drilling-induced magnetization and from normal-polarity present-day (late Quaternary) field remanence are observed and could often be easily removed during initial demagnetization steps. Instead, normal (N) or reversed (R) polarity could be indicated by NRM, pointing downward (N) or upward (R). The present-day magnetic field direction is -11.11° declination and 64.88° inclination (from https://www.ngdc.noaa.gov/geomag-web/#igrfwmm for the modern Knapps

Narrows corehole location), which should be roughly the same as the Eocene since no major continental movement has occurred.

2.2.3 Bulk isotope stratigraphy and age model

Percent CaCO3 was determined using a UIC CM140 coulometer. In this system approximately 20 mg of sediment is dissolved in 2 N sulfuric acid. For isotope analyses of bulk carbonate, a mass of ground sediment was weighed to obtain 35 and 50 μg of carbonate. All samples were analyzed with a Kiel IV Carbonate Device paired with a Thermo Scientific MAT253 Mass Spectrometer. The analytical precision of this system based on replicate analyses of Carrera Marble standards is better than 0.05‰.

2.2.4 Age Model

An age model was constructed for this section on the basis of carbon isotope stratigraphy, specifically the carbon isotope excursion (CIE) minima and maxima (H1, H2) correlated to the age model of Laurentano et al. (2016). This age model was then used to calculate sedimentation rates. (Table 1) The density of tie points using this approach limits our ability to constrain relatively short-lived changes in sedimentation rates.

2.2.5 Palynology

For quantitative palynological analysis, 18 samples were processed at Utrecht University. Between 3 and 15 g of freeze-dried, lightly crushed sediment was spiked with a known amount of exotic *Lycopodium* spores and subsequently treated with 30% HCl and twice with ~38–40% HF to dissolve carbonates and silicates,

respectively. The residue was sieved using 15 and 250 μm nylon mesh sieves, with ultrasonic bath steps to break up agglutinated organic matter. The resulting 15–250 μm palynomorph fraction was mounted on glass microscope slides. A general characterization of palynofacies, palynomorphs categories (pollen, spores, aquatic algae) and organic walled dinoflagellate cysts (dinocysts) in particular, was performed with light microscopy, counting at least 200, and typically >250 elements. For taxonomy, we refer to that cited in Williams et al. (2017), with the exception of Wetzelielloid taxa (see Bijl et al., 2016). For paleoecological reconstructions, dinocyst taxa are grouped in complexes of related species and genera with similar paleoecological affinities following the empirically-based complexes of Frieling and Sluijs (2018).

2.2.6 Clay Mineral Analysis

Clay mineralogy, bulk carbonate and benthic foraminiferal stable carbon and oxygen isotope analysis was performed in the Earth and Planetary Sciences Department at the University of California, Santa Cruz. For the clay mineral analysis, methods were adapted from Kemp et al. (2016), Gibson et al. (2000), and Poppe et al. (2001). Samples were lightly crushed and placed in a 1% sodium hexametaphosphate (Calgon) solution adjusted to a pH of 7–7.5 via the addition of ammonium hydroxide. Samples were placed on a shaker table at approximately 200 rpm for 48 hours to disaggregate the samples. Samples were then wet sieved through a 63 μm sieve to separate the coarse and fine fraction. Samples were then marked 5 cm from the surface of the solution and shaken to resuspend the clay minerals. The suspension was

allowed to rest for 4 hours and 6 minutes at 20°C in accordance with Stoke's Law. The suspension above the 5 cm mark was then extracted via syringe in order to isolate the <2μm fraction. This suspension was then dried down, and approximately 150 mg of this clay-sized fraction was then measured and resuspended in deionized water. The suspension was then passed through a sub-micron filter attached to a vacuum apparatus in order to remove the water from the suspension and orient the clays. The filter paper was removed and placed on the side of a glass beaker before being transferred to a glass slide to produce an oriented mount. For the glycolation step, mounts were placed inside a desiccation chamber with ethylene glycol at 60°C for a minimum of 4 hours.

These mounts were scanned in a Philips 3040/60 X'pert Pro X-ray diffraction unit from 0-35° 2θ with a 1-degree source beam and a 1/16 degree receiving slit at 45 mA and 40 mV. The results were then printed, and individual sample peaks were weighed to provide a semi-quantitative measurement of clay mineral abundances.

2.2.6 Foraminifer Oxygen Isotope Paleothermometry

Temperatures based on benthic oxygen isotopes and TEX_{86} were estimated following protocol outlined in Hollis et al. (2019). For oxygen isotopes, the paleotemperature equation of Marchitto et al. (2014) was used. For analyses of benthic foraminifera 4-6 Anomalinoides acutus specimens were picked from the 180-250 μm size fraction at each interval. All samples were analyzed with a Kiel IV Carbonate Device paired with a Thermo Scientific MAT253 Mass Spectrometer. The analytical precision of this system based on replicate analyses of Carrera Marble standards is better than

0.05‰. In order to calculate an absolute temperature, bottom-water $\delta^{18}O_{SW}$ was estimated based on the relationship between salinity and $\delta^{18}O$ established by Fairbanks (1982) and the modern-day salinity measurements reported in Richaud et al. (2016), with a -1.2‰ correction applied to account for the lack of ice during the Early Eocene. The largest source of error associated with the $\delta^{18}O$ temperature measurements is the uncertainty associated with local $\delta^{18}O_{SW}$. According to the Fairbanks (1982) equation, a change in salinity of ±1 psu when propagated across calculations can result in an error in temperature on the order of ±2.9°C. This error cannot be assumed to be constant throughout the core, as hydroclimate is expected to change dramatically during this time period, which could impact local salinity, as often seems to be the case with the PETM. However, agreement in trends between proxies suggests this effect is minimal.

2.2.7 TEX_{86} biomarker paleothermometry

For TEX_{86} analysis at Utrecht University, glycerol dialkyl glycerol tetraether (GDGT) lipids were extracted from ~10 g of powdered, freeze-dried sediment (18 samples) in 25 ml solvent mixture of dicholormethane (DCM):methanol (MeOH) (9:1, v/v) by a Milestone Ethos X Microwave Extraction System, set to 70 °C for 50 minutes. Filtered (using NaSO4 column) total lipid extracts were dried and separated in apolar, neutral and polar fractions through AlOx column chromatography, with hexane/DCM (9:1), hexane/DCM (1:1) and 1:1 DCM/MeOH (1:1), respectively as mobile phases, dried again and weighed. Polar fractions, after addition of a GDGT standard (99 ng of m/z 744) for quantitative analyses, were diluted in hexane/isopropanol (99:1) to a

concentration of 2 mg/ml. A 10 µl aliquot was filtered (0.45 µm polytetrafluoroethylene) and analyzed by high-performance liquid chromatography (HPLC) coupled to ionization mass spectrometer. Analytical precision was 0.006 TEX_{86} units, determined using an in-house GDGT standard. We use several indices to constrain potential confounding effects such as GDGT contributions from methanogenic/methanotrophic microorganisms, terrestrial sources and deepwater archaea. TEX_{86} values were calculated from isoprenoid GDGT abundances following Schouten et al. (2002) and converted to sea surface temperature (SST) using linear and exponential calibrations (e.g., Kim et al., 2010; O'Brien et al., 2017). Calibration errors are in the order of ±2.5°C (1 SD), but any offset from this calibration is assumed to be a constant throughout the study section.

3. Results

3.1 Stratigraphic Framework

A distinct magnetic reversal pattern is preserved in Knapps Narrows core with the lower section below 99.21 m (sample KN37) exhibiting a reversed polarity and the upper section (above 91 m, sample KN36) a normal polarity (Figure 2, 3). The reversal boundary, identified as the transition from magnetochron C24r to C24n based on nannoplankton stratigraphic data, thus lies within 99.21–91 m. According to nannoplankton data, the lowermost section is placed in lower Zone NP10 based on the first occurrence (FO) of *Rhomboaster* spp. and the absence of *Tribrachiatus contortus*. Upper Zone NP10 is identified at 96.6 m by the FO of *T. contortus* and basal Zone NP11 is identified at 95.1 m by the last occurrence of *T. contortus* along

with the presence of *T. orthostylus*. This reconstructed biomagnetostratigraphy (Supplemental Figures 1, 2) is generally consistent with the Paleogene time scale 2020 (Speijer et al., 2020) and timing of ETM2 (Cramer et al., 2003; Lourens et al., 2005; Westerhold et al., 2007; Stassen et al., 2012a).

The bulk carbonate carbon isotope record captures a -1.5‰ excursion from 98.18-96.41 m before recovering to the baseline followed by a second -3‰ excursion between 95.37- 93.46 m that peaks at 94.48 m (Figure 2). This "double peak" feature facilitates the recognition of ETM2, as it is documented for both marine and continental sections (e.g., Walvis Ridge and Bighorn Basin, Figure 2; Cramer et al., 2003; Stap et al., 2010, Abels et al., 2015). Between 93.46 and 88.98 m, carbon isotopes return to near baseline values before another -1.5‰ excursion at 88.51 m, consistent with observations of H2 at other sites (Figure 2; Cramer et al., 2003; Stap et al., 2010, Abels et al., 2015). Benthic foraminiferal values largely track bulk carbonate values. A low carbonate interval (Figure 3) coincides with the CIE minima at 94.48 m, where the sediments were barren of foraminifera.

3.2 Palynology

Palynological associations are dominated by marine palynomorphs, notably organic-walled dinoflagellate cysts (dinocysts) and common to abundant organic linings of benthic foraminifera. Terrestrial palynomorphs such as pollen and spores are rare. Dinocyst assemblages are well preserved and diverse and comprise a typical Paleogene shelf assemblage given abundant contributions of *Spiniferites* spp., *Operculodinium* spp, and species grouped in the *Areoligera* complex and

Cordosphaeridium cpx (e.g., Pross and Brinkhuis, 2005; Frieling and Sluijs, 2018). *Senegalinium* cpx, particularly abundant in the lower part of the section, tolerated low salinities (e.g., Brinkhuis et al., 2006), suggestive of strong seasonal river runoff, which seems contradictory to the absence of terrestrial pollen and spores.

Dinocyst abundance variability shows surprisingly little correspondence to climatic trends. For example, the *Apectodinium* complex, which includes *Apectodinium* spp. that show (quasi-)global abundance peaks across the PETM (Crouch et al., 2001; Frieling and Sluijs, 2018) demonstrates a small relative increase during the prior to ETM2 with their highest relative abundances occurring several meters above both ETM2 and H2 (Figure 4). The only anomaly that clearly corresponds to climate change is the peak abundance of epicystal Goniodomideae during H2. Also benthic foraminifer linings show anomalous abundances in this interval. Goniodomideae represent a thermophile group thriving in lagoonal environments (variable salinity) and further offshore under strongly stratified conditions (e.g., Reichart and Brinkhuis, 2004; Frieling and Sluijs, 2018).

3.3 Clay Mineralogy

Clay mineralogy showed moderate variation through the studied interval. However, these variations were not correlated with other proxies, and the timing of the mineralogic changes were offset relative to the carbon isotope excursions of ETM2 and H2, i.e. the shift in mineralogy begins prior to the CIE of ETM2 and after the CIE of H2. There is a marked increase in illite during the body of ETM2, and an

additional increase in the illite/smectite ratio immediately prior to H2 (Figure 3). There is no detectable kaolinite within the studied interval.

3.4 Oxygen Isotope Paleothermometry

Benthic foraminiferal $\delta^{18}O$ indicates a rise in bottom water temperatures of 1.5°C from 11.0°C (+2.8/-2.8, assuming a salinity change of 1 psu) to 12.5°C (+2.9/-2.9). Peak warming seems decoupled from minimum δ13C values for both ETM2 and H2 (Figure 3). These temperatures exceed bottom water temperatures during ETM2, which were measured to be 11.6°C (+2.9/-2.8), 0.9°C warmer than the baseline value. The greatest temperature increases are seen following the CIE associated with H2 at 14.4°C (+3.0/-2.9), 2.3°C warmer than the baseline. Given the resolution of the record, these temperature variations are likely the minimum estimates.

3.5 TEX_{86} Biomarker Paleothermometry

GDGT distributions indicate a dominant pelagic Thaumarchaeotal source based on low abundances of terrestrial GDGTs of and lipids derived from methanotrophs or methanogenetic microorganisms (Supplement Figure 4). GDGT2/3 ratios between 1.6 and 2.1 (Supplemental Figure 5) indicate dominant lipid origin from the upper ~100 meters of the water column (Hurley et al., 2018). Although this may imply contributions from sub-thermocline Thaumarchaeota potentially compromising direct quantitative SST assessment based on the surface sediment calibration dataset (Van der Weijst et al., in revision), we present the results as SST reconstructions following various linear and non-linear calibrations following convention (Hollis et al., 2019).

Variability in the TEX_{86} record should reflect SST variability very well (Ho and Laepple, 2016).

Sea surface temperatures based on TEX_{86} vary by a few degrees, largely mirroring the benthic bottom water temperature trends (Figure 3). Similarly, temperatures appear to increase prior to the body of ETM2 during the pre-onset excursion. Using a linear calibration, SST reached a maximum of ~30°C, ~1.1°C higher than the baseline. Exponential calibrations result in slightly lower SSTs and slightly muted warming (SI). TEX_{86} reaches minimum values during the CIE associated with ETM2, at ~28°C, 1.0°C colder than baseline values. The trend reverses and reaches a maximum following the CIE associated with H2 at ~ 31°C, ~1.3°C warmer than the baseline value.

4. Discussion

4.1 Stable carbon isotope signature

In comparison with the PETM sections spanning ETM2 in marine shelf settings are somewhat rare. Thus, the discovery of two smaller hyperthermals, ETM2 and H2, on the mid-Atlantic coast along with the PETM provides a unique opportunity to assess how regional climate responded to two distinct levels of greenhouse forcing. Apart from bio-chronostratigraphy, key to identifying ETM2 is the stable carbon isotope stratigraphy, specifically the presence of paired negative excursions ETM2 and H2, which at Knapps Narrows is broadly consistent with trends observed elsewhere. Similar to the PETM, marine carbonates of ETM2 contain a smaller excursion than those observed in continental sections (Tipple et al., 2011; Stap et al., 2010;

Westerhold et al., 2018; Abels et al., 2015). This has been attributed to dissolution during the peak of the PETM in marine sections dampening the marine signal or changes in soil conditions, humidity or plant communities and physiology enhancing the terrestrial signal (Bowen et al., 2004; Tipple et al., 2011; Sluijs and Dickens, 2012). The magnitude of the carbon isotope excursion here is intermediate to records of the ETM2 in open marine and continental settings, but is consistent with observations of the PETM carbon isotope excursion in marginal marine settings (John et al., 2008; Tipple et al., 2011; Sluijs & Dickens, 2012). Although the interval with low carbonate content prevented the generation of a more detailed foraminiferal isotope record, the covariance between the bulk carbonate and the benthic foraminiferal $\delta^{13}C$ throughout combined with the biostratigraphy and magnetostratigraphy confirms our interpretation of the carbon isotope stratigraphy.

4.2 Acidification and siliciclastic flux

The PETM in the study region is characterized by a clay or low carbonate layer which has been attributed primarily to climatically driven enhanced siliciclastic sediment fluxes (Gibson et al., 2000; Kopp et al., 2009). High-resolution climate simulations are consistent with enhanced precipitation, which likely elevated erosion and sedimentation (Rush et al., 2021). Similarly, there are two potential explanations for the low carbonate interval associated with the body of ETM2. Coastal acidification would dissolve carbonate preventing its burial. It is unlikely that elevated CO_2 levels alone could drive this given the rates of estimated C emissions (e.g. Harper et al., 2020). It is possible that this effect could be enhanced by enhanced oxidation of

organic matter, both in situ and transported into the shelf (Bralower et al., 2018; Lyons et al., 2019). Enhanced siliciclastic transport, on the other hand, is likely the main cause but to a much lesser extent with an estimated 50-100% increase in rates during ETM2 (compared to 10x with the PETM). Although the coarse resolution might not capture a brief increase in sedimentation rates, our age model indicates age model shows sedimentation rates remained fairly constant, ranging from 4.6 to 10.8 cm/kyr. The lowest rates occurred prior to ETM2, and the highest occurred during the background state between ETM2 and H2 (Figure 6). This being an expanded section, other factors may have a role in observed sedimentation rates, such as the paleobathymetry. As the studied interval overlies a disconformity, it is possible there was a localized depression that was more readily filled than the surrounding area (Supplemental Figure 3). Additionally, sedimentation rates in shelf settings can vary on timescales shorter than our age model is able to account for, with the model only capturing the average over long time periods. It is possible that the observations are an amalgamation of periods of enhanced sedimentation and non-deposition (Trampush &Hajek, 2017).

4.3 Temperature

There is broad correlation between the observations of temperatures derived from TEX_{86} and $\delta^{18}O$, suggesting the derived variations are accurate. TEX_{86} records indicate minor variations with a rise of 1°C prior to ETM2, a drop of 1°C relative to the baseline during the body, and an increase of 1.3°C during H2. In contrast, paleotemperature reconstructions from the PETM derived from TEX_{86} and $\delta^{18}O$ at

other sections in the region suggest 5–8 °C surface warming without much scatter (Sluijs et al., 2007; Zachos et al., 2006; Babila et al., 2022) (Figure 5). The elevated temperatures prior to the CIE associated with ETM2 is followed by a drop in temperatures during the event. There are multiple potential explanations for the apparent lack of correspondence between the CIEs and temperature variability. In any shelf setting, deposition is generally discontinuous and variable, particularly during periods of dramatic climatic changes such as Eocene hyperthermals (Trampush and Hajek, 2017). This has the potential to introduce preservation and sampling biases within the sedimentary record, and given the coarse resolution of the temperature records, the remote possibility of not capturing a warming anomaly on the order of a few tens of thousands of years. Another possibility is the contribution of regional scale changes resulting from changing ocean and atmospheric circulation patterns in a modestly warmer world. With modern warming, for example, it is predicted that changes to the Atlantic Meridional Ocean Circulation would result in regionally lower temperatures in the North Atlantic (Jackson et al., 2015). Another factor to consider is orbital forcing. The Eocene hyperthermals appear to coincide with 400-kyr eccentricity maxima (Lourens et al., 2005; Zachos et al., 2010). Although the lower frequency cyclical changes in CO2 appear to be paced by eccentricity (Zeebe et al., 2017), depending on the phase of precession, local temperature, particularly on or near land, could deviate from global patterns (Kiehl et al., 2018). This effect would be further exaggerated if local sediment deposition tended to be biased toward one phase. The variation in responses between various proxy systems and muted

responses relative to the PETM highlights the nonlinearity of the climate system to CO2 forcing and demonstrates the importance of considering additional forcings. The ETM2 has already been documented in numerous pelagic sections, which uniformly demonstrate warming during the event (Harper et al., 2018). The uniformity observed in open ocean sections is mirrored in previously documented shelf sections. The central Lomonosov Ridge has been argued to have experienced an increase in warm, wet conditions during ETM2, similar to reconstructions for the PETM (Sluijs et al., 2009; 2020). TEX86 records for this site indicate a warming on the order of 3-5°C.

4.4 Hydrological Cycle

Evidence supporting a modest intensification of the hydrologic cycle includes the shift in clay mineralogy from smectite-dominated facies to illite-dominated facies during the body of ETM2, as well as a moderate increase in illite prior to H2. Clay mineralogy has been used extensively as a proxy for chemical weathering, with a spectrum from smectite to illite to kaolinite being associated with increasingly wet and warm conditions (Singer, 1980). While previous studies on clay mineralogy over the PETM in this region have demonstrated noted increases in kaolinite (Gibson et al., 2000), sediments contained in this interval contained no detectable levels of kaolinite. Many locations experience a dramatic increase in kaolinite during the PETM (Robert & Kennett, 1994; Gibson et al, 2000; Kemp et al., 2016; Chen et al., 2016). Previous work in the study area points to the reworking of older deposits as the source of kaolinite (Gibson 2000; John et al., 2012). However, other regions have

been argued to demonstrate an authigenic weathering response to the PETM (Clechenko et al., 2007; Chen et al., 2016). Furthermore, work on the radioisotopes of the clay minerals, namely strontium and lead, demonstrate little change in the sourcing of sediment in this region during the PETM (Rush et al., in prep). Additionally, recent work on lithium isotopes seems to suggest changes to global weathering patterns during the PETM (Pogge von Strandmann et al., 2021; Ramos et al., 2022). Illite being a product of weathering intermediate to smectite and kaolinite, its presence within this section seems to support the interpretation that the clays formed in situ during ETM2. As would be expected, the environmental perturbations during ETM2 would likely illicit a weathering response intermediate to the background state and that of the PETM.

Abundances of the low-salinity-tolerant *Senegalinium* cpx and the supply of terrestrial palynomorphs have pointed to increase river run off in shelf sections across hyperthermals (e.g., Crouch et al., 2003; Sluijs and Brinkhuis, 2009; Sluijs et al., 2009). However, *Senegalinium* abundances show no correspondence to the CIEs or temperature anomalies. It was abundant before, during and after ETM2. It did not return during H2 after its gradual decline, which does not support a strong hydrological response to this event. Terrestrial palynomorphs are rare throughout the record, reminiscent of the upper Paleocene and lower Eocene of the New Jersey Shelf (e.g., Zachos et al., 2006). It suggests that the hinterland was barely vegetated in the region, also explaining the lack of response during the PETM, ETM2 and H2. This may be consistent with the paleolatitude of about 33°N (van Hinsbergen et al., 2015).

In contrast to the records here, the Lomonosov Ridge palynological assemblages demonstrate a marked shift, with an increase in dinoflagellate markers for freshening and eutrophication as well as palm pollen indicating high winter temperatures (Sluijs et al., 2009). Further evidence of hydrologic changes is noted in hydrogen isotope records of leaf wax n-alkanes, which demonstrate a large rise during the PETM (Pagani et al., 2006) a rise prior to ETM2, and a drop during the body of the event as well as during H2 (Krishnan et al., 2014). Similar records of enhanced siliciclastic flux were also archived at Mead and Dee Streams in New Zealand across several hyperthermal events (Nicolo et al., 2007; Slotnick et al., 2012). While focused more on biotic and ocean chemistry conditions, the Nile Basin is also interpreted as having a similar response to the PETM but on a smaller scale (Stassen et al., 2012a). Such evidence of enhanced hydrology driving siliciclastic fluxes is also found in hemipelagic sections such as the Terche section of northeastern Italy (D'Onofrio et al., 2016).

The records from continental sections suggest changes in the regional precipitation patterns were not entirely uniform. An increase in siliciclastic sediment flux in a terrestrial section at Ellesmere Island is interpreted as evidence of an intensified hydrologic system during ETM2 (Reinhardt et al., 2022). However, the Bighorn Basin record suggests contrasting regional climatic changes between the PETM and earlier hyperthermal events (Abels et al., 2016), in line with observations from this study.

4.5 Environmental and depositional setting

Palynological assemblages present a more complicated story. The overall assemblages are typical of those seen in coastal, open marine neritic settings. They show plenty of variability in fresh-water run-off, stratification and productivity, but the majority of these changes shows no relation to δ13C or temperature change.
A shallowing trend in the upper section of the core may be discerned from a long-term decline in the abundance of the low-salinity-tolerant *Senegalinium* cpx and a rise of the Goniodomids. which typically occur in massive (harmful) blooms in (seasonally) high salinity, warm, lagoonal conditions in modern and ancient settings (Zonneveld et al., 2013; Frieling and Sluijs, 2018; Sluijs et al., 2018). Overall, the trends from the *Senegalinium* complex and Goniodomids may indicate a shift from brackish conditions to more saline conditions in younger portions that do not necessarily correspond to hyperthermal events and may well indicate an overall longer-term trend. However, Goniodomids reach a maximum at H2 that also corresponds to the highest reconstructed temperatures. A rise in salinity seem to precede this warming but it should be noted that dinoflagellate blooms are strongly seasonal and therefore should not necessarily correspond to our salinity estimates.
The correspondence of Goniodomid abundances with transient global warming events has been previously recorded, for example in brief intervals of the PETM on the New Jersey Shelf (Sluijs and Brinkhuis, 2018), and the Nigerian Shelf (Frieling et al., 2018) and across the Middle Eocene Climatic Optimum in the eastern equatorial Atlantic (Cramwinckel et al., 2020). Very high stable carbon isotope ratios suggest these Goniodomid abundances indicate that at least some of these abundances

represent an increase in the geographical range and frequency of harmful blooms (Frieling et al., 2017; Sluijs et al., 2018).

Additionally, abrupt transitions within the distribution patterns of several species, including the *Apectodinium* cpx, here dominantly representatives of *Wetzeliella* spp., but also other elements like remains of microforaminiferal linings, suggest minor disconformities, condensed sections, or depositional hiatuses that would result in highly variable sedimentation rates below the resolution able to be recorded based on the carbon isotope age model. Terrestrial palynological markers are sparse throughout the core, which would imply overall low plant biomass in the catchments, despite intensification of the hydrological cycle.

On balance the overall hydrologic response to ETM2 appears much more modest than reconstructed for the PETM, and somewhat less than expected given the scale of global warming and assuming a roughly linear response of precipitation patterns to global warming. Given that the baseline temperature prior to ETM2 is a few degrees higher than prior to the PETM, it is possible that sensitivity to an equivalent temperature perturbation would be less extreme than for the PETM, i.e. a state dependent response. This also suggests variability in hydroclimate responses to greenhouse forcing in different regions. While the Artic records demonstrate a strong hydrological response across ETM2 (Sluijs et al., 2009), here the interpretation is less straightfoward. Depending on the region, local hydroclimate seems to respond in a somewhat non-linear fashion to global warming, characterized more by abrupt mode shifts (e.g., frequency of extremes, or duration of wet vs. dry seasons) as opposed to

gradational changes (e.g., mean annual precipitation). In this region, our palynological record appears to confirm this overall 'mild' response to the ETM2; in effect, to record only minor changes is rather unique, given that other transient climatic events in the Cenozoic are typically characterized by massive coeval concomitant dinocyst assemblage changes.

5. Conclusions

This study provides the first documented identification of ETM2 and H2 in the Salisbury Embayment of the mid-Atlantic Coastal Plain. Clay mineralogy, $\delta^{18}O$, and TEX_{86} records portray climate perturbations across this interval. The shift in clay mineralogy from smectite to illite taken in the context of kaolinite dominated facies during the preceding PETM suggests the clay mineralogy changes are authigenic and represent an intermediate stage of weathering relative to the PETM and the background state resulting from an enhanced hydrologic cycle. Temperature proxies show minor increases in temperature, that appear asynchronous with changes to the carbon cycle and may represent alternative forcings such as changes in ocean and atmospheric circulation or orbital forcing or a potential sampling artifact. Dinocyst assemblages demonstrate little response to the short-lived hyperthermals and point more towards being dominated by long-term trends. When compared to the PETM and other records of ETM2, these contrasting records demonstrate the complexities of climatic changes and regional variability associated with rapid warming events, highlighting the need for extensive spatial coverage to interpret climatic changes. In essence, the local Δprecipitation did not scale linearly with the Δtemperature. Future

research into high-resolution climate models of these smaller scale hyperthermal events may assist in interpretation of this record as well as records in different regions.

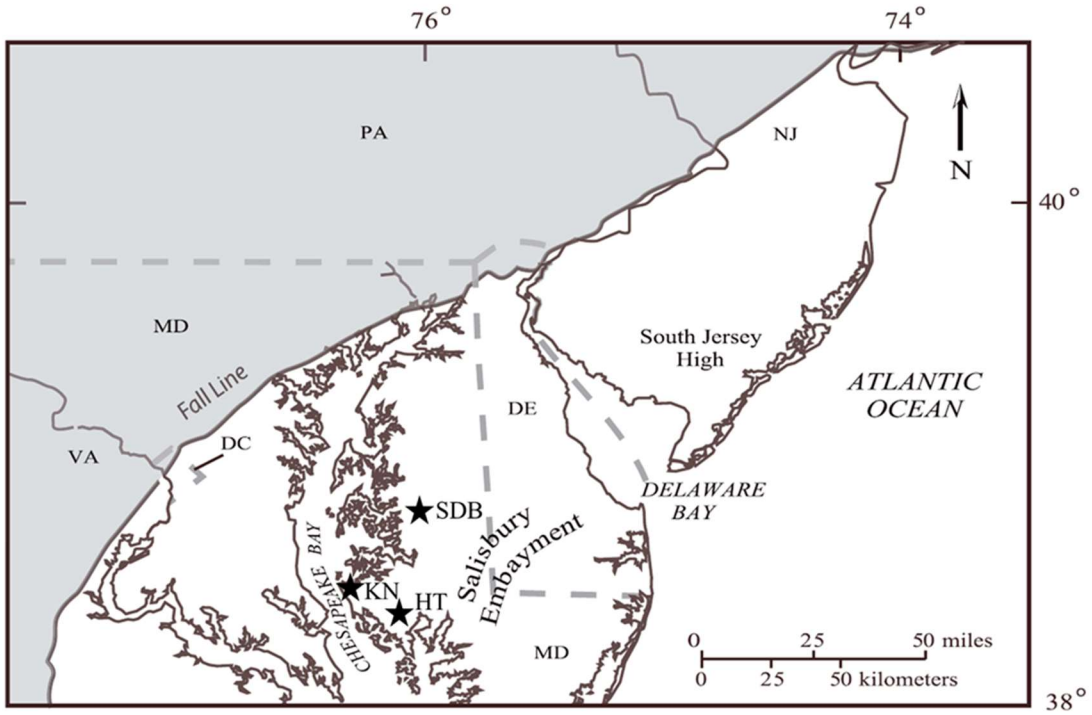

Figure 1: Map showing location of the Knapps Narrows (KN), South Dover Bridge (SDB), and Howards Tract coreholes. Fall Line represents the shift between crystalline basement rock and Cretaceous-Cenozoic sediments. Modified from Self-Trail et al. 2017.

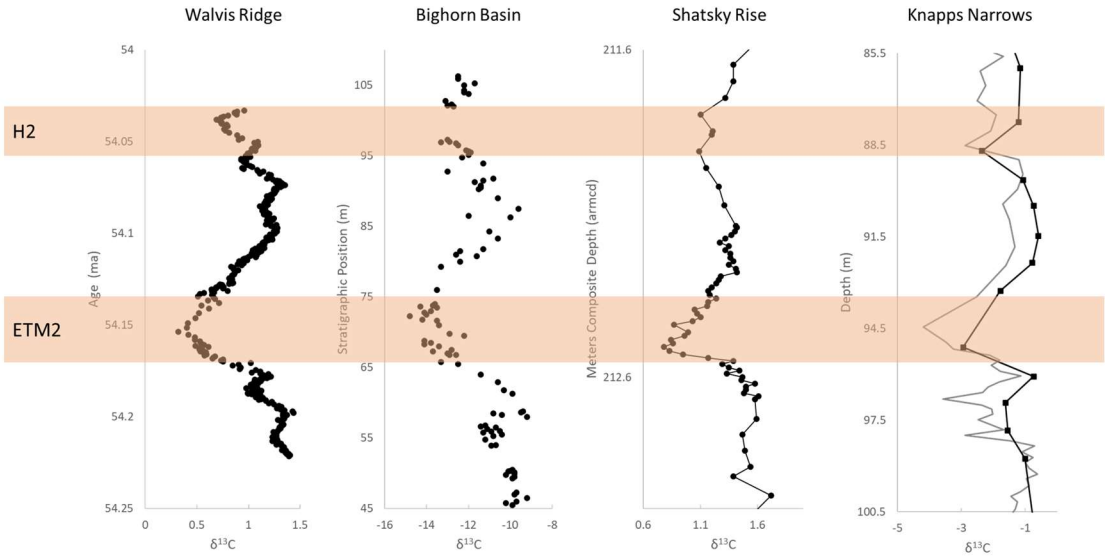

Figure 2: Carbonate $\delta^{13}C$ records of ETM2 and H2 at Walvis Ridge (bulk), Bighorn Basin (pedogenic nodules), Shatsky Rise (benthic), and Knapps Narrows (this study). For Knapps Narrows, bulk carbonate values are in gray and benthic values are in black. Knapps Narrows at 94.5 m was nearly barren of foraminifera. Walvis Ridge data from Stap et al., (2010), age model from Lauretano et al., (2016), Bighorn Basin from Abels et al., (2015), and Shatsky Rise from Westerhold et al., (2018).

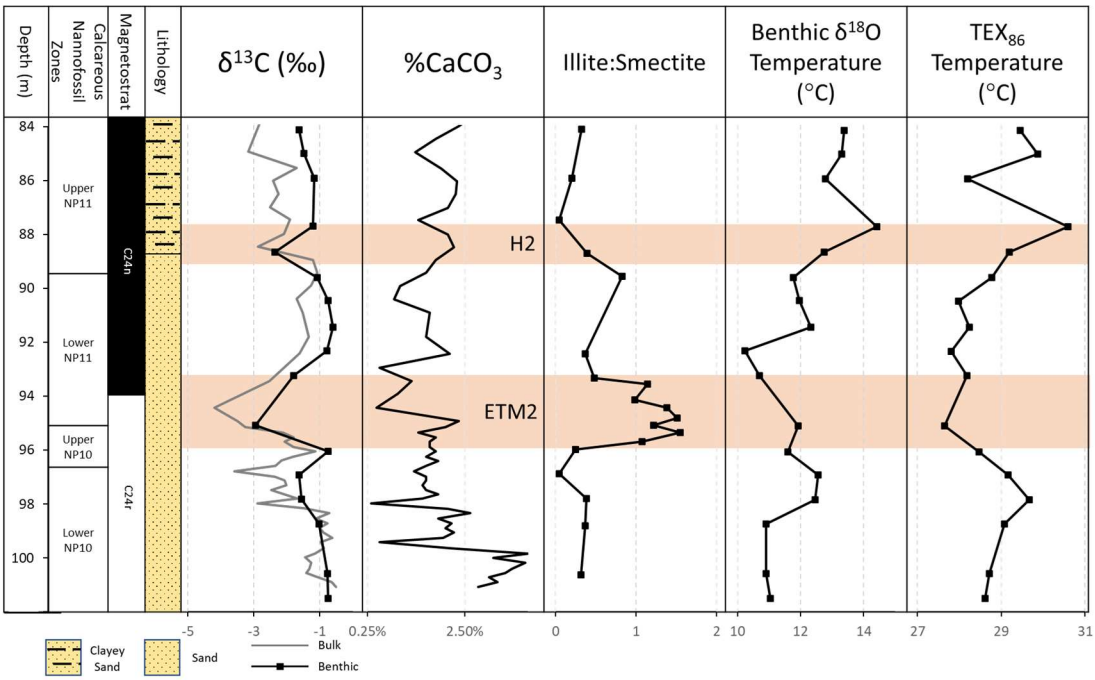

Figure 3: From left to right: depth, nannofossil zones, magnetochrons, lithology, carbon isotopes, % carbonate, clay mineralogy, benthic $\delta^{18}O$ temperatures, and TEX_{86} sea surface temperatures over the ETM2 and H2 interval at Knapps Narrows. TEX_{86} temperatures use linear calibration from O'Brien et al., (2017). Note logarithmic scale for % carbonate and low carbonate interval at ETM2, spike in illite-smectite ratio at ETM2, agreement between benthic and sea surface temperatures, as well as offsets in timing between carbon isotopes, clay mineralogy, and temperature proxies.

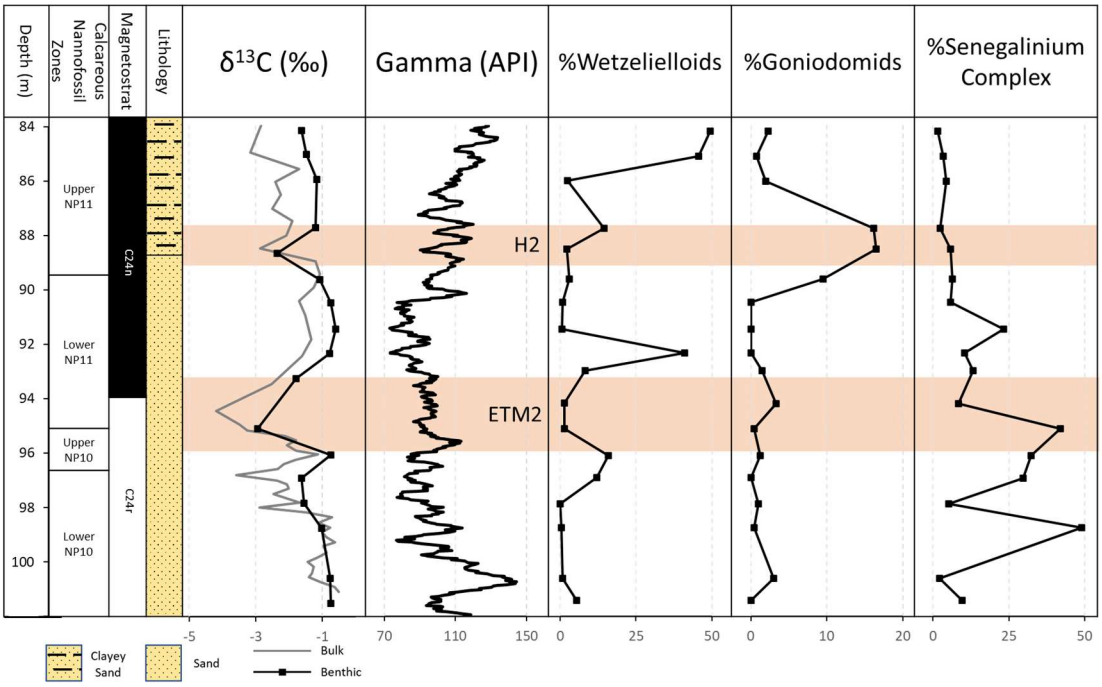

Figure 4: From left to right: depth, nannofossil zones, magnetochrons, lithology, carbon isotopes, wireline gamma, relative abundance of Wetzelielloids, relative abundance of Goniodomids, and relative abundance of the Senegalinium Complex. Fluctuations in gamma are associated with relative abundance of clay minerals and may be associated with higher-order cyclostratigraphy. Wetzelielloids are associated with periods of high productivity, Goniodomids are associated with high temperatures and strong salinity stratification, and the Senegalinium complex is associated with low salinity (Frieling and Sluijs, 2018). Of note is a long-term increase in salinity from relatively fresh conditions at the base of the core to more saline conditions upsection. Rapid changes in abundance of Wetzelielloids suggests disconformities, periods of non-deposition, or condensed sections.

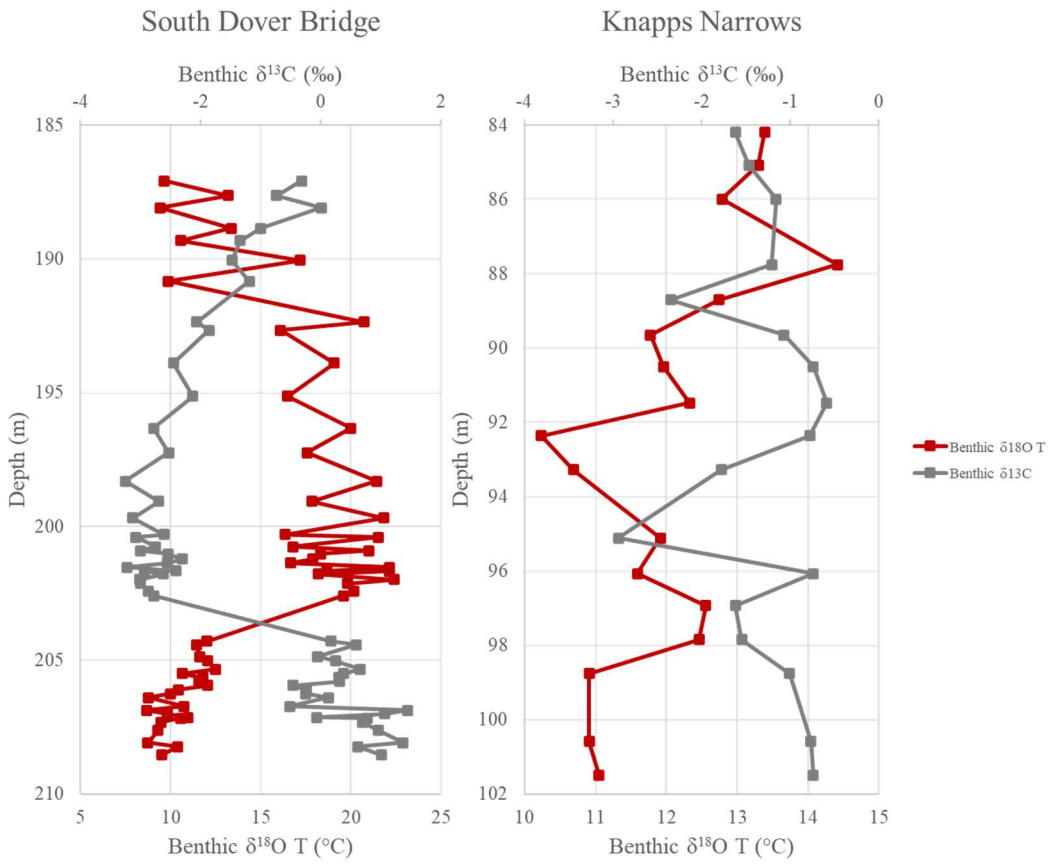

Figure 5: Comparative benthic $\delta^{13}C$ and $\delta^{18}O$ derived temperatures from the PETM interval of South Dover Bridge core (data from Babila et al., 2022) and ETM2 within the Knapps Narrows core. Both cores are from the Eastern Shore of Maryland. Note strong correlation between temperature shifts and carbon isotope excursion during PETM at South Dover Bridge and relative lack of correlation at Knapps Narrows.

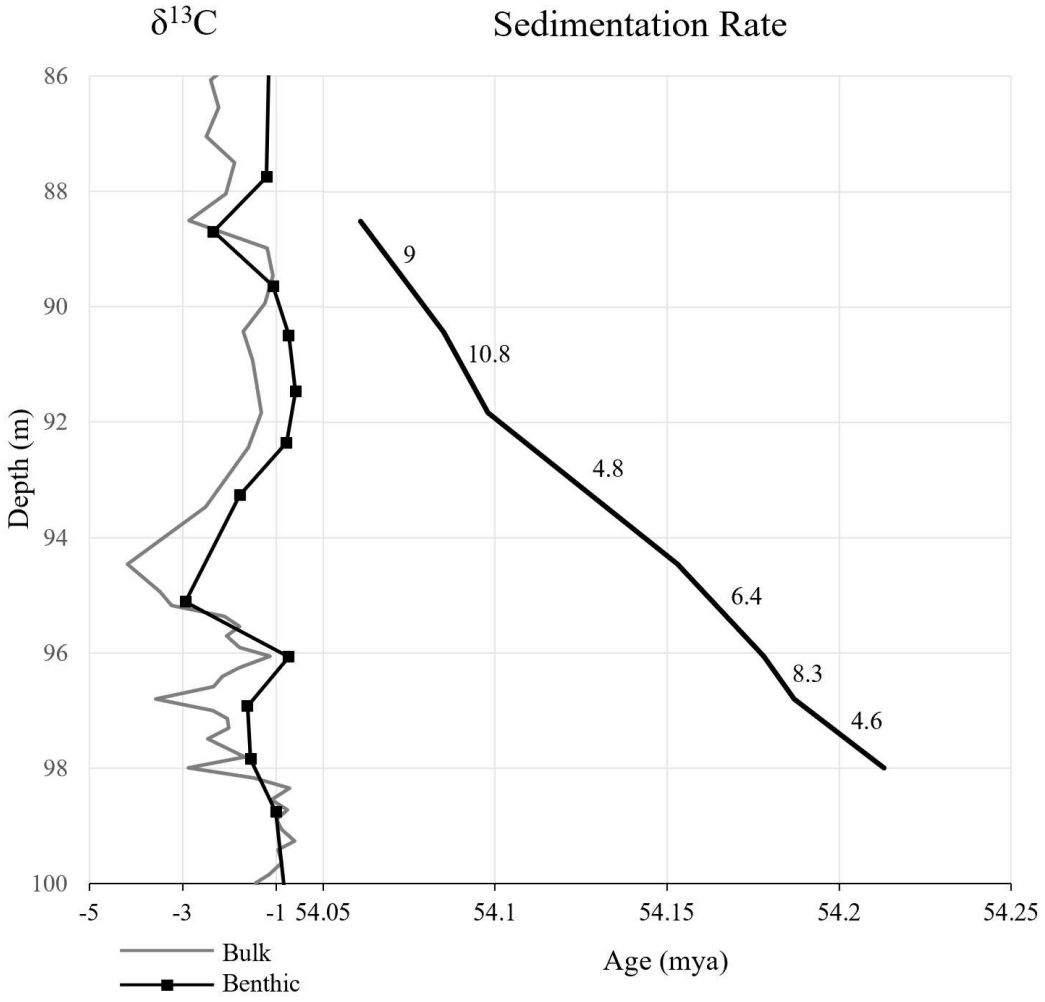

Figure 6: Sedimentation rates in the Knapps Narrows core based on correlations of δ13C inflection points to the age model of Lauretano et al., 2016 at Walvis Ridge Site 391. Sedimentation rates in cm/kyr. Note relative consistency compared to orders of magnitude changes that were documented during the PETM in Stassen et al., 2012b.

	Depth (m)	Walvis age model (mya)	Sed rate (cm/kyr)	Distance from ETM2 (m)	Age from ETM2 (kyr)
ETM2 $\delta^{13}C$ peak 1	97.99	54.213		-3.54	-60
ETM2 $\delta^{13}C$ peak 2	96.80	54.187	4.57	-2.35	-34
preETM2 max	96.06	54.178	8.30	-1.60	-25
ETM2 $\delta^{13}C$ min	94.46	54.153	6.40	0	0
ETM2 recovery max	91.87	54.098	4.77	2.62	55
Interlude min	90.43	54.085	10.79	4.02	68
H2 peak 1	88.51	54.061	8.98	5.94	92

Table 1: Age model and tie points used in reconstruction of sedimentation rates.

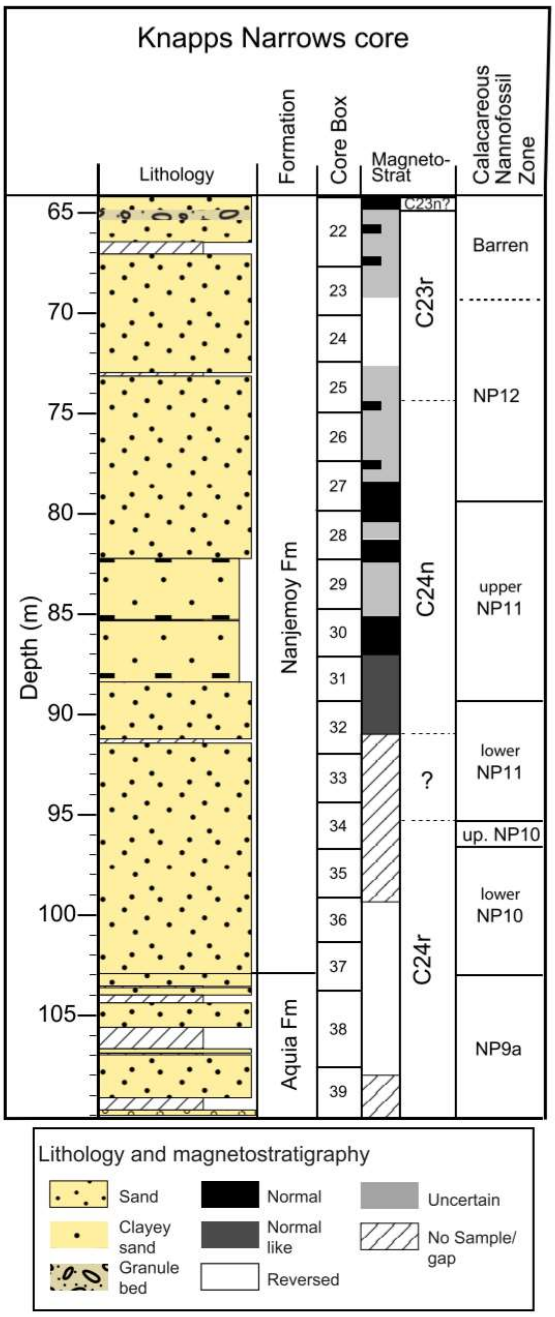

Supplemental Figure 1: The magnetostratigraphy and nannofossil zones of Knapps Narrows core. Note that the C24r/C24n reversal boundary was not well determined

due to a sampling gap, but was well constrained to the interval, where the question mark was placed, based on nannofossils.

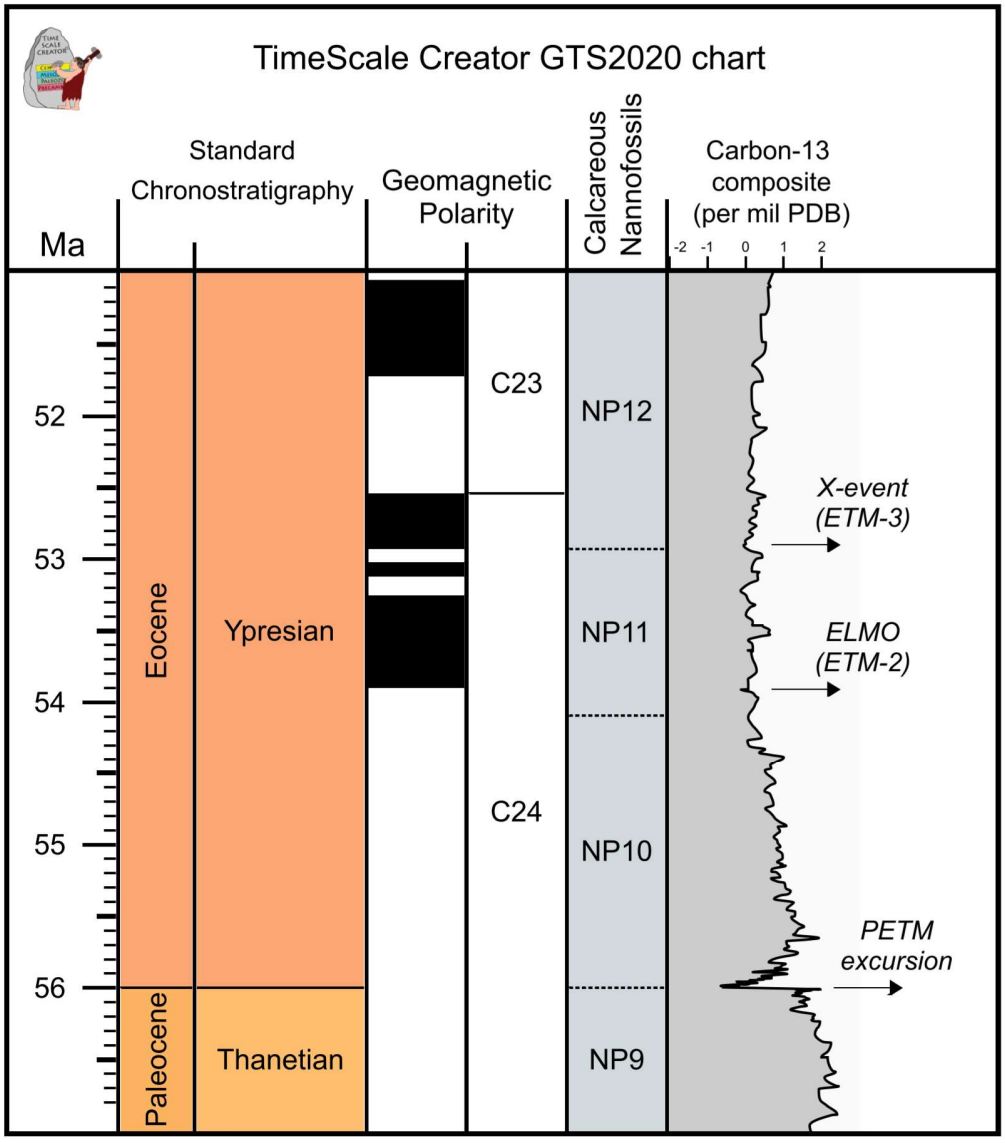

Supplemental Figure 2: The latest Paleocene to earliest Eocene time scale from GTS2020 (Gradstein et al., 2020) showing the geomagnetic polarity scale, the calcareous nannofossil zones and the composite carbon-13 isotope curve (major

carbon-13 excursions and events are also marked). The excursion of ETM2 aligns with the C24r/C24n reversal.

Gradstein, Felix M., James G. Ogg, Mark D. Schmitz, and Gabi M. Ogg, eds. Geologic time scale 2020. Elsevier, 2020.

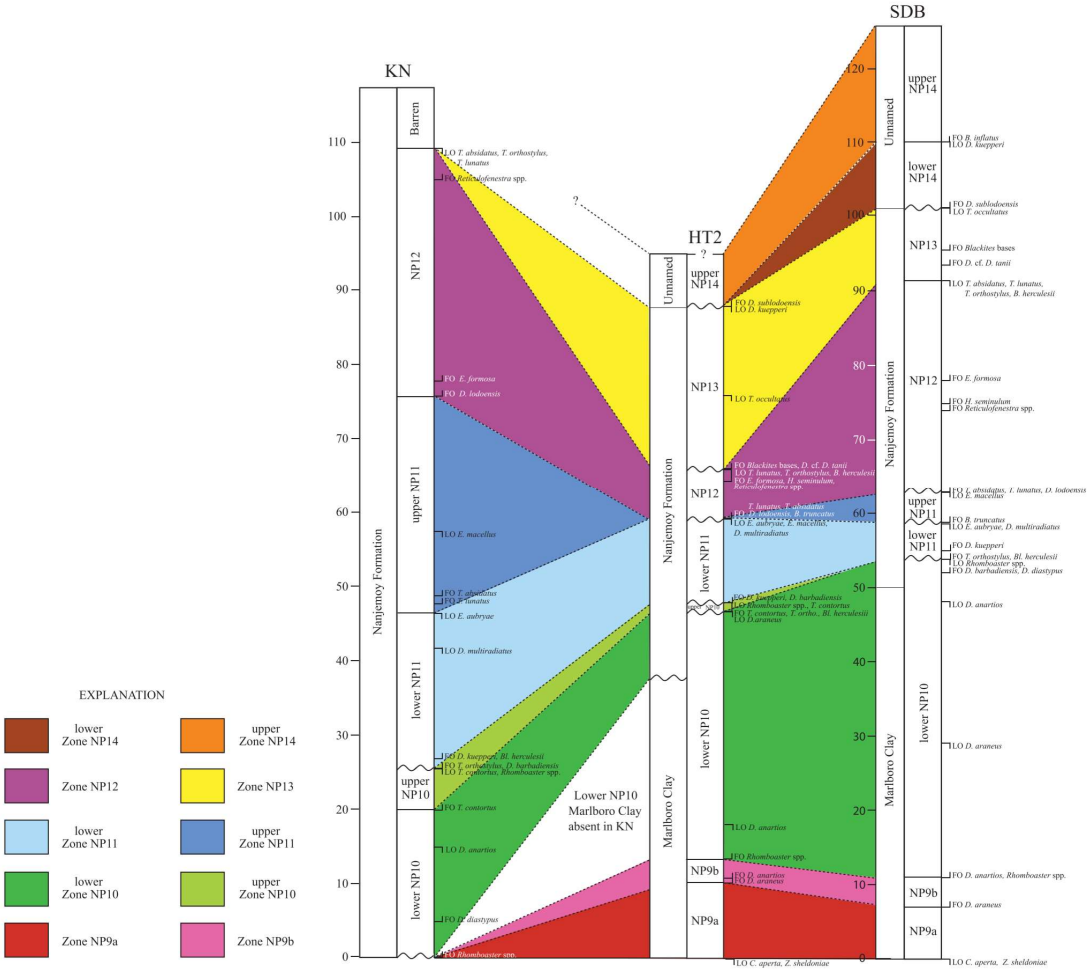

Supplemental Figure 3: Regional calcareous nannofossil biostratigraphy. Locations from figure 1. Note disconformity at base of Knapp's Narrows as indicated by lack of Lower NP10.

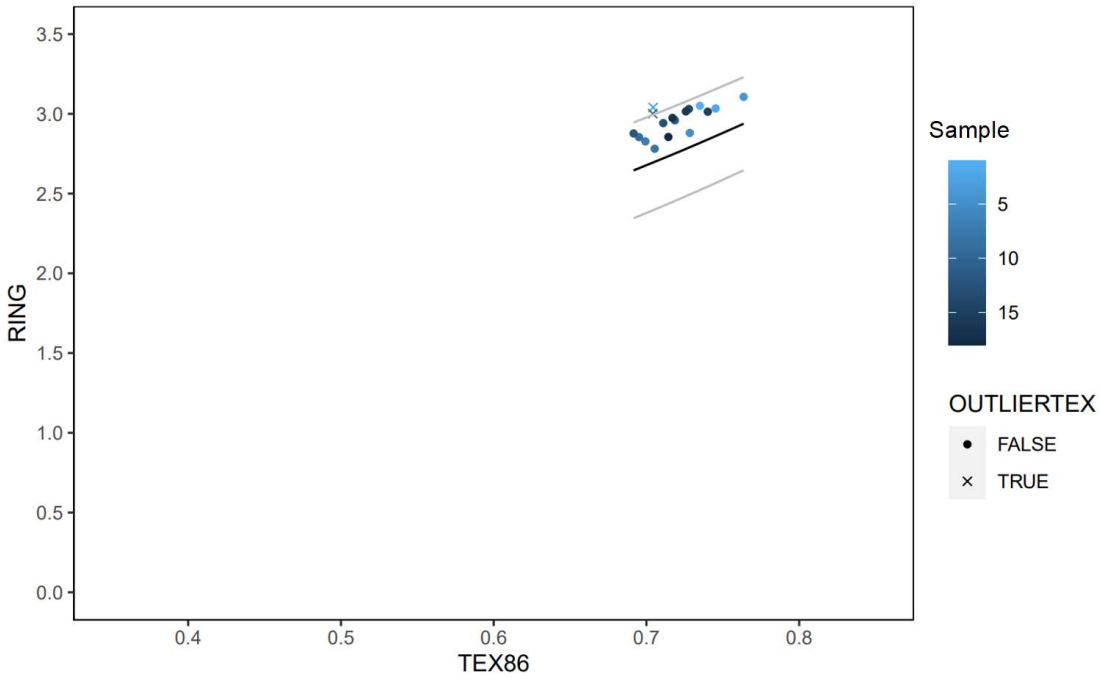

Supplemental Figure 4: Ring index plotted against TEX86 values for Knapps Narrows. Values generally fall within the acceptable range, indicating little terrestrial overprint. The temperature reconstructions obtained from the outliers were in line with independent measurements from δ18O, and thus were kept in the previous figures.

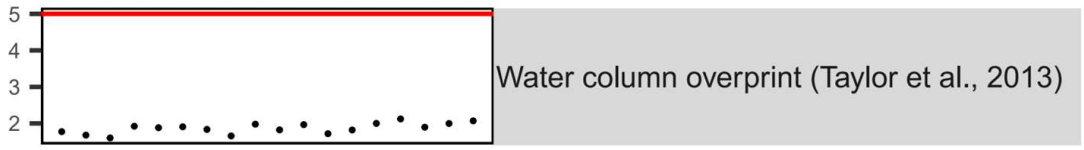

Supplemental Figure 5: GDGT2/3 ratios of samples from Knapps Narrows. Values between 1.6 and 2.1 indicate dominant lipid origin from the upper ~100 meters of the water column.

Continuous Sediment Sourcing and Changes in Weathering during the PETM in the Salisbury Embayment

William Rush[1], James Zachos[1], Terrence Blackburn[1], Philip Pogge von Stradmann[2], Pratigya Polissar[1], Noah Finnegan[1]

[1]Department of Earth and Planetary Sciences, University of California Santa Cruz, 1156 High Street, Santa Cruz, CA 95064, USA

[2]Mainz Isotope and Geochemistry Centre, Institute of Geosciences, Johannes Gutenberg University, 55122 Mainz, Germany

ABSTRACT

The Paleocene-Eocene Thermal Maximum, or PETM, was a period of rapid warming that occurred ca. 55.5 mya. This resulted in dramatic changes to regional climates including warming between 5-8°C and substantial changes in precipitation patterns. Marginal marine sediments deposited during this time show a marked increase in kaolinite content often viewed as evidence of increased chemical weathering attributed to climate driven shifts in the intensity and latitude of precipitation. It remains unclear, however, whether this kaolinite formed during the PETM or was a reworked from older deposits thus representing a shift in physical transport. Here, we utilize lithium isotopes in a mid-Atlantic margin shallow marine section, South Dover Bridge, to characterize changes in weathering congruency as well as strontium and lead isotopes to constrain changes in provenance. Lithium isotopes demonstrate a negative ~3‰ excursion interpreted as a decrease in residence time, and while there is variation in the strontium and lead isotopes, they are largely within the bounds of the proposed kaolinite source, the late Cretaceous Raritan formation, not only during the PETM, but during the late Paleocene and the recovery as well. These results are interpreted as an increase in both physical weathering and chemical alteration taking place during the PETM, driven by enhanced temperatures and hydrologic activity, with a relatively constant sediment sourcing.

INTRODUCTION

The Paleocene-Eocene Thermal Maximum, or PETM (55.5 million years ago) is considered one of the best analogues to modern-day anthropogenic warming.

Although the exact magnitude and timing are debated, it is estimated that between 4,500 to over 10,000 Pg carbon were released on the order of 10,000 years (Zeebe et al., 2009; Gutjahr et al., 2017). In response, global temperatures rose by approximately 5°C triggering dramatic mode shifts in regional hydroclimates as expressed by marked changes in sediment lithology and accumulation rates and other proxies of precipitation (Schmitz and Puljate, 2007; John et al., 2008; Carmichael et al., 2018;). In particular, numerous regions have demonstrated an increase in kaolinite content, including Antarctica, Spain, China, and the Mid-Atlantic Coast of the United States (Robert & Kennett, 1994; Pujalte et al., 2015; Chen et al., 2016; Gibson et al., 2000). Generally, kaolinite is known to form under warm, wet conditions with intense chemical weathering. However, in many locations in which kaolinite is found during the PETM, it is argued to have been a result of enhanced physical erosion. Yet there is debate as to whether kaolinite could form authigenically during the PETM itself (John et al., 2012; Chen et al., 2016). At least one region suggests in-situ formation of kaolinite during the PETM due to the presence of mudcracks in a kaolinite-dominated paleosol (Clachenko et al., 2007). Previous attempts to characterize the sourcing of the kaolinite in the Mid-Atlantic region have argued for reworking during the PETM on the basis of oxygen isotopes of the clay fraction of sediments and the presence of thermally mature organic material within PETM sediments (John et al., 2012; Lyons et al., 2019). The former study is limited in that it was not able to account for the fractionation factor between clay species as well as the shifts in oxygen isotopes that occur during periods of hydrologic disruption (Savin & Epstein, 1970; Edwards et al.,

1996). While the latter study was not focused on the clay fraction, it is possible that the organic material may be subject to preservation bias due to high erosion and sedimentation rates during the PETM, and relatively low rates in the late Paleocene (Stassen et al., 2012).

This study will seek to better characterize siliciclastic weathering in the mid-Atlantic Salisbury Embayment during the PETM by means of tracking provenance via Pb and Sr isotopes as well as tracking changes in weathering congruency utilizing lithium isotopes. It is hoped that in doing so we may gain a better understanding of the regional hydrologic response to rapid warming as well as better understand weathering feedbacks. We focus on one of several Paleocene-Eocene sections cored within the Salisbury Basin, South Dover Bridge (SDB), Maryland. Previous studies on this core have produced detailed chemo-, litho and biostratigraphic records thus establishing the duration and magnitude of the PETM as well as relative changes in local sediment fluxes. The primary patterns are verified with records from a section located further south in the basin, Howards Tract.

To quantify the degree chemical weathering, we utilize lithium isotopes as a proxy. The dissolution of primary minerals drives δ^7Li of formation waters lower, whereas secondary mineral precipitation drives δ^7Li values higher as the lighter ^{6}Li isotope is preferentially incorporated into secondary mineral formation. This balance between dissolution and removal is known as weathering congruency. Past studies demonstrate that the Li isotopic composition of clay minerals reflects the isotopic composition of the waters they form in with a negative (α=0.986) offset (Pistiner &

Henderson, 2003; Pogge von Strandmann et al., 2021). Therefore, by analyzing the lithium isotope of the clay minerals, we can gain insight into the weathering conditions at the time of formation.

GEOLOGIC SETTING

The Salisbury Embayment was a broad shallow extension of the Atlantic Ocean over what is now Eastern Virginia, Maryland, Delaware, and Southern New Jersey. The region contains a sequence of sedimentary units ranging from the Cretaceous through the present, underlain by crystalline basement rock. The lithology through the late-Paleocene and early-Eocene in western Maryland as represented in SDB consists of the late-Paleocene Aquia Formation, a clayey, silty, glauconitic sandstone which transitions into the Marlboro Clay, a clay-rich unit with variable amounts of silt, in the early Eocene, before transitioning into the Nanjemoy Formation, a clayey, silty, glauconitic sandstone similar to the Aquia Formation which was deposited following the recovery from the PETM. The Marlboro Clay conformably overlies the Aquia formation, with the base marked by a distinct carbonate-free interval that also coincides with the base of the global carbon isotope excursion (CIE) across the entire basin (see Stassen et al., 2012). There is a disconformity of varying degrees between the Marlboro Clay and the Nanjemoy Formation (Self-Trail et al., 2017; Bralower et al., 2017).

Two cores were utilized in this study, South Dover Bridge, herein referred to as SDB, and Howards Tract, referred to as HT. The Howard Tract section was drilled in the Eastern Shore of Maryland at 38.4483, -76.1416, about 35 km to the southwest

of South Dover Bridge, located at 38.747, -76.007. The Paleocene-Eocene boundary was recovered at SDB at a depth of 202.59 m, and at HT at 200.35 m.

METHODS

A 25-meter section of SDB and HT were sampled for this study. Sample preparation, carbonate content, $\delta^{13}C$, XRD clay mineralogy, radiogenic isotope analysis, and trace metal analysis were performed at the University of California, Santa Cruz. Lithium isotope measurements were performed at University College London. Samples of the Raritan Formation were acquired from the University of Pennsylvania to test as a potential source.

For the clay mineral analysis, methods were adapted from Kemp et al. (2016), Gibson et al. (2000), and Poppe et al. (2001). Samples were lightly crushed and placed in a 1% sodium hexametaphosphate (Calgon) solution adjusted to a pH of 7–7.5 via the addition of ammonium hydroxide. Samples were placed on a shaker table at approximately 200 rpm for 48 hours to disaggregate the samples. Samples were then wet sieved through a 63 μm sieve to separate the coarse and fine fraction. Samples were then marked 5 cm from the surface of the solution and shaken to resuspend the clay minerals. The suspension was allowed to rest for 4 hours and 6 minutes at 20°C in accordance with Stoke's Law. The suspension above the 5 cm mark was then extracted via syringe in order to isolate the <2μm fraction. This suspension was then dried down, and approximately 150 mg of this clay-sized fraction was then measured and resuspended in deionized water. The suspension was then passed through a sub-micron filter attached to a vacuum apparatus in order to

remove the water from the suspension and orient the clays. The filter paper was removed and placed on the side of a glass beaker before being transferred to a glass slide to produce an oriented mount. For the glycolation step, mounts were placed inside a desiccation chamber with ethylene glycol at 60°C for a minimum of 4 hours. These mounts were scanned in a Philips 3040/60 X'pert Pro X-ray diffraction unit from 0–35° 2θ with a 1-degree source beam and a 1/16 degree receiving slit at 45 mA and 40 mV. The results were then printed, and individual sample peaks were weighed to provide a semi-quantitative measurement of clay mineral abundances.

The lithium isotope composition of the clay sized fraction of sediment was analyzed at University College London following the methods outlined in Pogge von Strandmann et al., 2021.

Radiogenic isotope and trace metals were determined on samples from SDB. For the analyses, approximately 200 mg of each sample was leeched according to the procedure outlined in Tessier et al. (1979) in order to remove carbonates, oxides, and organics, leaving only the siliciclastic fraction. To account for the changing lithology, the clay-sized fraction was used, while the Raritan was processed in bulk to account for the weathering of larger minerals. Samples were then dissolved in 6 ml concentrated HF and 0.2 ml concentrated HNO_3 inside of an Anton Paar Multiwave GO Microwave Digestion System. Samples were then treated with 2.5 N HCl saturated with H_3BO_3 to dissolve any fluoride precipitates.

Lead was purified first, using a dilute HBr anion exchange column chemistry. Strontium was purified using a Sr-spec resin. For the lead, samples were brought up

in 6 ml of 0.5 N HBr. Columns were loaded with 0.2 ml of anion resin, then cleaned with 12 ml of 4 N HNO3, 12 ml of 0.5 N HNO3, and 1 ml Milli-Q water. Columns were then conditioned with 1 ml of 0.5 N HBr before loading the sample. Samples were then washed with 2.6 ml of 0.5 N HBr with the eluate being collected for strontium column chemistry. Samples were treated with 2 ml of 0.5 N HNO_3 to release the lead.

To isolate the strontium, samples were first dried down, then brought up in 0.5 ml of 7 N HNO_3. Columns were loaded with 0.5 ml of strontium specific resin. The resin was cleaned with 10 ml of 0.1 N H_2SO_4, rinsed with 10 ml of Milli-Q water, and preconditioned with 1 ml of 7 N HNO_3 prior to loading the samples. The samples were then rinsed with 3 ml of 7 N HNO_3. Samples were then treated with 0.05 N HNO_3 to release the strontium. Sr and Pb isotope analysis was carried out on a thermal ionization mass spectrometer (TIMS).

RESULTS

At SDB the onset of the isotope excursions occurs within the carbonate free layer marking the base of the Marlboro Clay. Nevertheless, both the foraminifer and bulk sediment oxygen and carbon isotope records capture in detail the main body of the oxygen and carbon isotope excursions (see Babila et al., 2022). Locally, based on the O isotopes SST warmed by more than 5°C as $\delta^{13}C$ decreased by >3.5‰. The relative thickness of the CIE indicates a significant increase in sedimentation rates and siliciclastic sediment fluxes, similar to other sections along the margin, wherein orders of magnitude increases have been documented during the PETM (Self-Trail et

al. 2017, Stassen et al., 2012). At HT, the isotope excursions also occur at the base of the Marlboro clay. The C isotope records shows anomalously low values due to the presence of siderite (Bralower et al., 2018).

A distinct shift in the clay mineralogy is manifested by an increase in kaolinite content rising from below detectable limits in the late Paleocene to greater than 25% during the body of the CIE (Figure 2). Clay sediments at South Dover Bridge demonstrate shifts in the lead and strontium isotopic composition across the Paleocene-Eocene boundary. Strontium isotopes demonstrate a similar shift to less radiogenic values at the P-E boundary which quickly recovers, but otherwise do not demonstrate a clear trend. Lead isotope ratios show a shift that tracks closely with the carbon isotope excursion. (Figure 2)

Range of values for the Raritan can be found in the table below:

	Min	Max
$^{87}Sr/^{86}Sr$	0.733	0.866
$^{207}Pb/^{206}Pb$	0.820	0.835
$^{208}Pb/^{206}Pb$	2.02	2.06

With limited exceptions, all samples of the clay-sized fraction of South Dover Bridge fall within the bounds. A notable exception being at the P-E boundary (Figure 2).

The SDB Lithium isotopes demonstrate an excursion on the order of 3‰ at the Paleocene-Eocene boundary. This transition initiates just prior to both the carbon

isotope excursion and change in clay mineral assemblages. A similar transition is observed at Howards Tract (Supplemental Figure 1).

DISCUSSION

To a first order, the local increase in siliciclastic sediment fluxes points toward a substantial change in the character of physical weathering and sediment transport, most likely brought about by changes in regional precipitation intensity, either overall mean annual precipitation or the seasonality of precipitation (i.e, more monsoonal) and/or in the frequency of short-term extreme events (John et al., 2008; Rush et al., 2021). Given the limitations of the sediment record, testing such hypotheses is challenging and requires multiple approaches. Therefore, this study has utilized lithium isotopes to track changes in weathering congruency and strontium and lead isotopes to track changes in provenance.

A shift toward greater seasonality (longer dry season, more intense shorter wet season) would affect the residence time of surface/sub-surface waters within catchments and thus chemical weathering intensity. Lithium isotopes, reflect the relative rates of dissolution of primary material to the precipitation of secondary materials (Pogge von Strandmann et al., 2021). However, this seemingly simple relationship is complicated by the fact that changes in the rates of either of these can have an impact on the lithium isotope composition of waters and in turn minerals that are precipitated by those waters. As documented by Dellinger et al., 2015 in the modern-day Amazon Basin, trends in lithium isotopes follow a “bell-shaped” pattern, wherein areas with low residence time of sediment within the system result in low

δ^7Li values due to high rates of denudation and dissolution relative to precipitation and somewhat counterintuitively areas with high residence times also result in low δ^7Li values due to reworking of previously precipitated material. These end members are categorized as supply-limited regimes wherein parent material is entirely weathered prior to transport and weathering-limited regimes wherein parent material is incompletely weathered prior to transport. Given the high sedimentation rates that existed during the PETM, it is likely that the sedimentation and erosion regime represented by the lithium isotope excursion during this time period would be more in line with the weathering-limited end member (Stassen et al., 2012). Furthermore, it is likely the higher temperatures associated with the PETM would have accelerated the chemical reactions associated with the weathering process, amplifying the hydrologic effects. It is worth noting that although this would indicate high rates of physical erosion with a low residence time of sediment relative to chemical weathering and precipitation of new minerals, this does not necessarily mean that the rate of formation of secondary minerals slowed during the PETM, rather simply that the increase in precipitation was outpaced by dissolution.

This change in the lithium isotope composition supports a shift in the regional seasonality and precipitation extremes and may also be influenced by changes to the water table depth and weathering profile. Previous modeling studies have demonstrated regionally enhanced seasonality and precipitation extremes in response to both changes in orbital forcing and CO_2 forcing (Rush et al., 2021). These flashier precipitation patterns could result in enhanced sediment transport with lower

residence times which would drive δ^7Li lower. Furthermore, recent studies have also demonstrated the impact of water table on weathering and δ^7Li values (Ramos et al., 2022; Golla et al., 2020). Enhanced seasonality can lead to a deepening of the water table, with well drained soils resulting in enhanced dissolution and weathering. One additional complication, due to the existing fractionation of previously formed secondary minerals, is that their dissolution and subsequent reprecipitation would result in further fractionation of the lithium isotopes. (Dellinger et al., 2015; Liu et al., 2015).

It is notable that the lithium isotope excursion at SDB begins prior to the carbon isotope excursion and change in clay mineralogy. This may be in part due to the similar enhanced seasonality and precipitation that occurs within the model at eccentricity maxima (Figure 4, Rush et al., 2021). This would be consistent with the interpretation of the PETM beginning at an eccentricity maxima (Zeebe and Lourens, 2019).

These observations of enhanced weathering and erosion as indicated by a negative lithium isotope excursion are not limited to this location, nor are they limited to the PETM. Pogge von Strandmann et al., (2021) found this lithium isotope excursion to be a global signal, with siliciclastic sections in Northern Europe demonstrating similar shifts in the lithium isotopes prior to the carbon isotope excursion. Additionally, Pogge von Strandman et al., (2013) found similar negative lithium isotope excursions associated with Cretaceous Ocean Anoxic Events. In both

instances, these are argued to have played an important role in the carbon drawdown and recovery from these events.

Regarding the provenance of the sediment, several studies have argued for extensive reworking of previously deposited sediments in this region during this period, on the basis of the time scales required for clay mineral formation (Thiry, 2000), oxygen isotopes of the clay mineralogy (John et al., 2012), as well as biomarkers that indicate older, thermally mature organic matter during the PETM interval (Lyons et al., 2019). The $^{207}Pb/^{206}Pb$, $^{208}Pb/^{206}Pb$, and $^{87}Sr/^{86}Sr$ ratios demonstrate excursions that track with the carbon isotope excursion and changes in clay mineralogy. However, these values are largely consistent with measured values from the Raritan and appear to show a mixing between a range of compositions observed within the Raritan itself (Figure 3). Furthermore, this agreement between the radiogenic isotopes of the Raritan Formation and South Dover Bridge suggests that the Raritan likely served as a primary source of sediment not only during the PETM, but during the late Paleocene and following the PETM as well. This hypothesis is further supported by the fact that the lithology of the surrounding region is dominated by igneous and metamorphic complexes that would be much more resistant to weathering than the loosely consolidated sediments of the Raritan, which would have been the only sediment body to the east of the Appalachian Mountains during the Paleocene.

This is significant to the debate of the “authigenesis” of the clays found in PETM deposits. As previously noted, the conventional interpretation of the shift in

clay mineralogy to kaolinite dominated facies is interpreted as a reworking of Cretaceous-aged laterite deposits (John et al., 2012). Regarding the previous studies on reworking of sediment in this region, John et al., 2012 based on the oxygen isotopes could not directly account for fractionation between different clay species (Savin & Epstein, 1970). Furthermore, given the degree of hydrologic change that is anticipated to have occurred in this region, it is possible these changes could have also influenced the oxygen isotope composition of new clays that formed. Lyons et al., 2019 found an increase in mature biomarkers within PETM sediments in the region and a paucity of biomarkers in Paleocene sediments, interpreting this as sourcing sediment from the Raritan during the PETM. However, during the late Paleocene it is possible that erosion and sedimentation rates were slow enough to allow for the reworked organic material to be weathered over longer time periods, while the orders of magnitude higher sedimentation rates during the PETM allowed for rapid burial and preservation.

Additionally, there exists some debate on the reworking question in other regions. A documented spike in kaolinite at the P-E boundary in lacustrine deposits in central China has been interpreted as being a local weathering product formed during the PETM based on constant carbonate content suggesting that no change in sediment fluxes occurred while the mineralogic makeup changed (Chen et al. 2016). Another potential site indicating enhanced alteration of secondary mineral formation exists in North Dakota, which radiometric dating of ash layers places at the Paleocene-Eocene boundary. At this site, a kaolinite-rich layer, as high as 84%, is argued to have formed

pedogenically from the enhanced alteration of pre-existing smectite-rich units due to a jointing structure associated with fragipan development as well as the lack of known kaolinite-rich units in underlying Cretaceous or early Paleocene sediments in the surrounding region (Clechenko et al., 2007). Ultimately, we are left with three possibilities: the kaolinite was reworked from previously formed kaolinite within the Raritan, it formed as a result of enhanced weathering of other siliclastics within the Raritan, or some combination of the two.

Previous studies have noted kaolinite within the Raritan formation (Thornburg et al., 2019). However, it was also noted to contain a variable amount of swelling clay. Of the Raritan samples analyzed for this study, all of them contained large amounts of swelling clays that prevented accurate measurements on the XRD as it was not possible to produce an oriented mount. Furthermore, studies of ETM2 in this region also show a shift in clay mineralogy, albeit to a makeup dominated by illite rather than kaolinite (Rush et al., in prep). Illite being an intermediate weathering product between the end members of smectite and kaolinite, this response in clay mineralogy to a smaller scale warming event suggests some degree of authigenesis rather than a simple reworking.

Furthermore, apart from the higher temperatures noted in this area during the PETM (Babila et al., 2022), climate model output of this region had demonstrated significant changes in precipitation patterns in response to both CO_2 and orbital forcing, resulting in both a change in seasonality and extremes of precipitation (Figure 4; see Rush et al., 2021). These changes to precipitation patterns would likely

result in significant changes to sediment erosion and transport, as well as driving changes in water table fluctuations and weathering profiles.

Given the above lines of evidence, the most plausible interpretation of changes in sedimentation during this period is both an enhanced sediment transport as well as an enhanced chemical weathering. It is likely that the Raritan Formation provided the source of sediment based on the radiogenic isotopes as well as the previous biomarker work. However, this does not preclude enhanced weathering during this time period resulting in enhanced kaolinite production, and these effects likely work in conjunction as the reduced residence time and enhanced transport worked to continuously expose fresh material for weathering, in a process referred to as the "weathering engine" (Anderson et al., 2004). When overburden is removed and fresh material is exhumed, minerals are removed from their equilibrium state at depth and are subject to more intense chemical alteration (NRC, 2001). This accelerated rate of weathering and leaching of iron from within the critical zone could have contributed to the formation of the bacterial magnetofossils associated with high-iron runoff found in PETM sediments in this region (Riebe et al., 2017; Kopp et al., 2009). As has been suggested previously in other locations, this enhanced weathering could contribute to the relatively rapid recovery observed following the PETM through enhanced carbon drawdown (Pogge von Strandmann et al., 2021).

CONCLUSIONS

This study analyzed the changes in lithium, strontium, and lead isotopes as well as the mineralogy of the clay-sized fraction of sediments in the South Dover

Bridge core during the PETM. During this interval, sediments demonstrate an increase in kaolinite content as well as a shift in radioisotope composition. However, changes are within the bounds of measured end members within the Raritan, suggesting little to no change in the source of sediments. Lithium isotopes also document a negative excursion which, taken in context of the higher sedimentation rates, is interpreted as a decrease in residence time of sediment within the catchment area, as fresh material was continuously exposed and rapidly weathered. This enhanced weathering could play an important role in the recovery from the PETM. The shifts in lithium isotopes prior to the carbon isotope excursion, similar to those seen elsewhere, suggest alternate forcings such as orbital variation play an important role in the weathering process. Coupling these observations to climate model output suggests an intensified weathering and erosion in response to more extreme precipitation patterns.

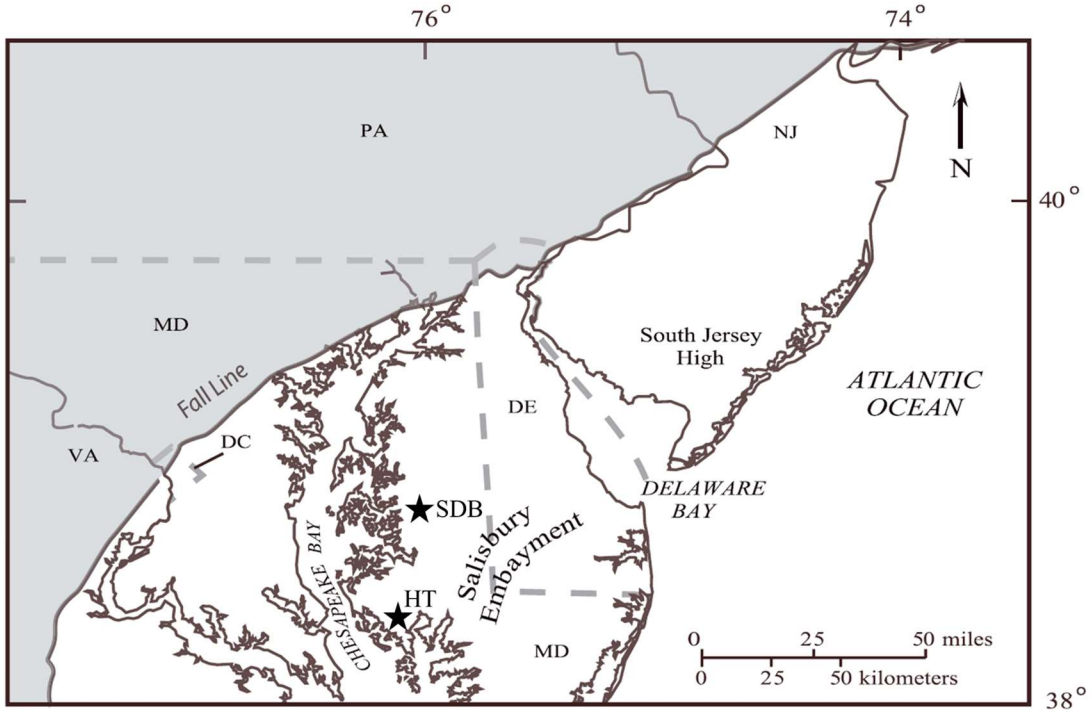

Figure 1: Map showing location of study sites, SDB and HT. Fall line represents shift from crystalline basement rock to Cretaceous through modern sediments. Modified from Self-Trail et al., 2017.

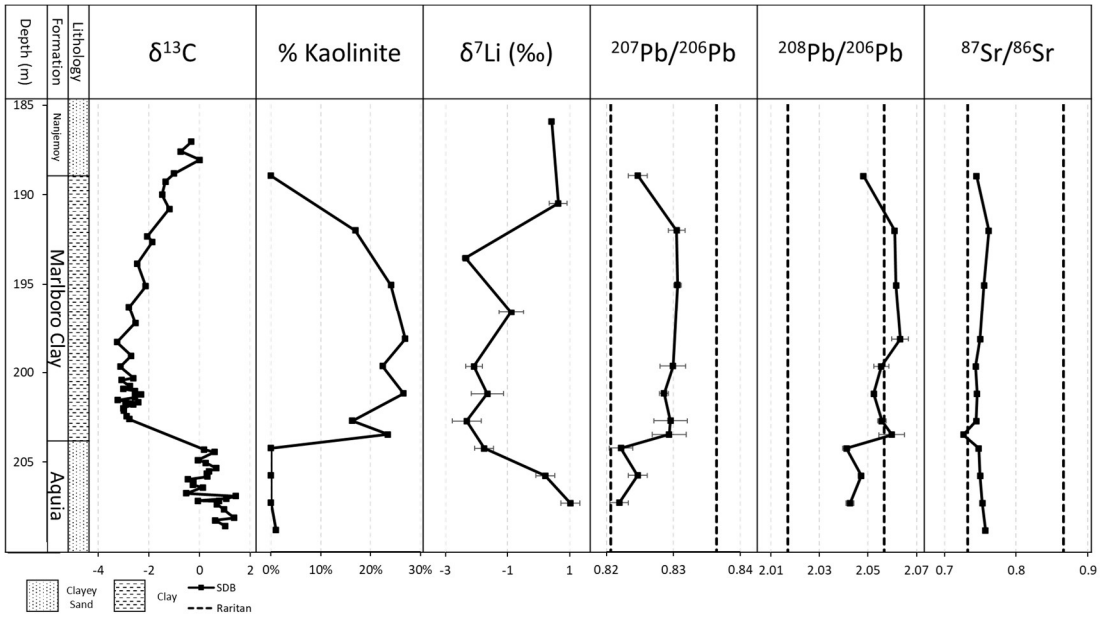

Figure 2: Lithology, benthic foraminiferal $\delta^{13}C$, % kaolinite of clay-sized fraction, $\delta^{7}Li$, $^{207}Pb/^{206}Pb$, $^{208}Pb/^{204}Pb$, and $^{87}Sr/^{86}Sr$ measurements from the clay-sized fraction of South Dover Bridge. Dashed lines represent Raritan end members. Error in $\delta^{7}Li$ reported as 2 standard deviations. Radioisotopes reported as percent standard error. Error in strontium isotopes is too small to resolve in figure. $\Delta^{13}C$ from Babila et al., 2022.

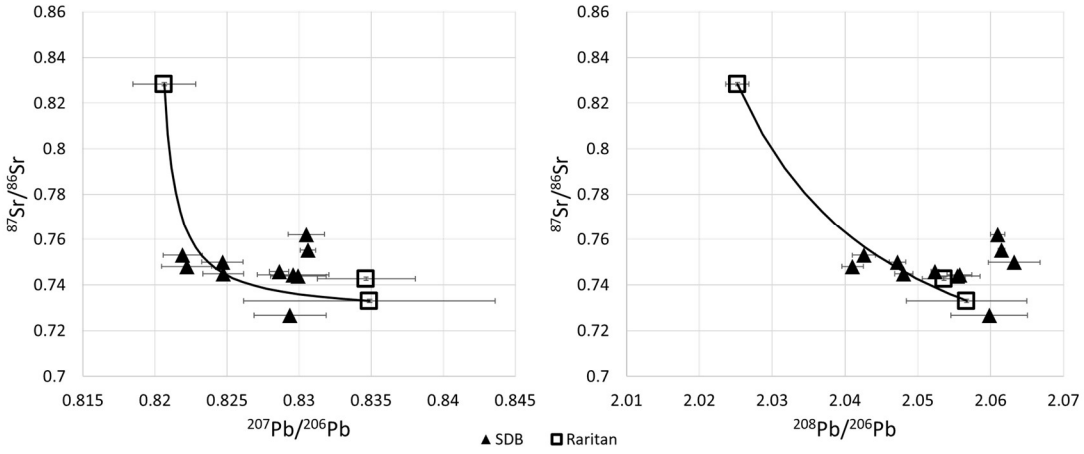

Figure 3: Crossplots of $^{207}Pb/^{206}Pb$, $^{208}Pb/^{206}Pb$, and $^{87}Sr/^{86}Sr$ from the Raritan formation and clay-sized fraction of South Dover Bridge. A weighted mixing model developed by Philips & Koch, 2002 is used. Note general agreement in South Dover Bridge clay composition and mixing between Raritan end members. Lowest strontium value outside of these bounds was taken at the PETM boundary. Line represents mixing model between measured Raritan values.

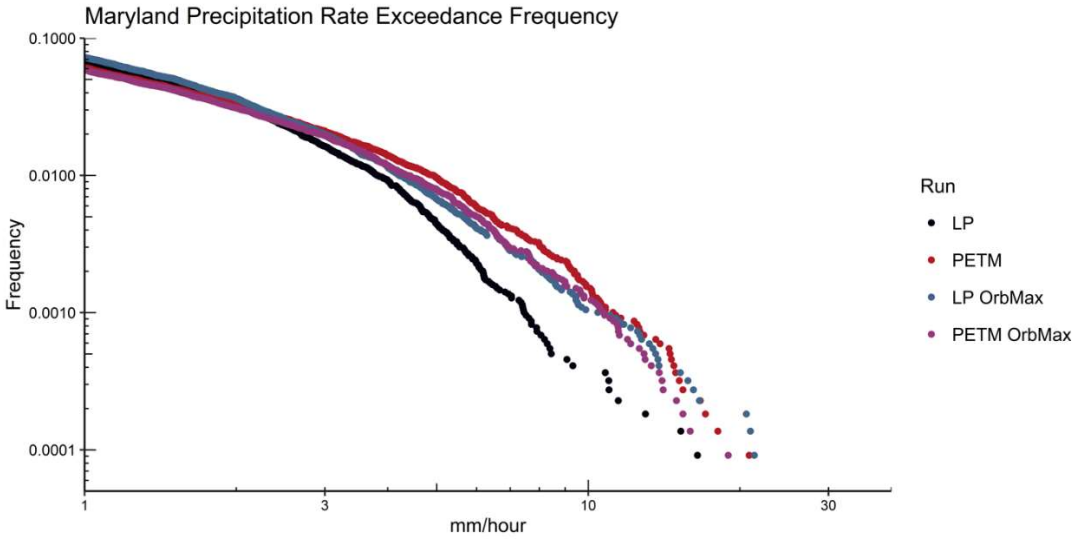

Figure 4: Exceedance frequency of precipitation from CAM5 climate model output of the study area. Full model details can be found in Rush et al., 2021. Note increase in extreme precipitation in response to both orbital and CO_2 forcing.

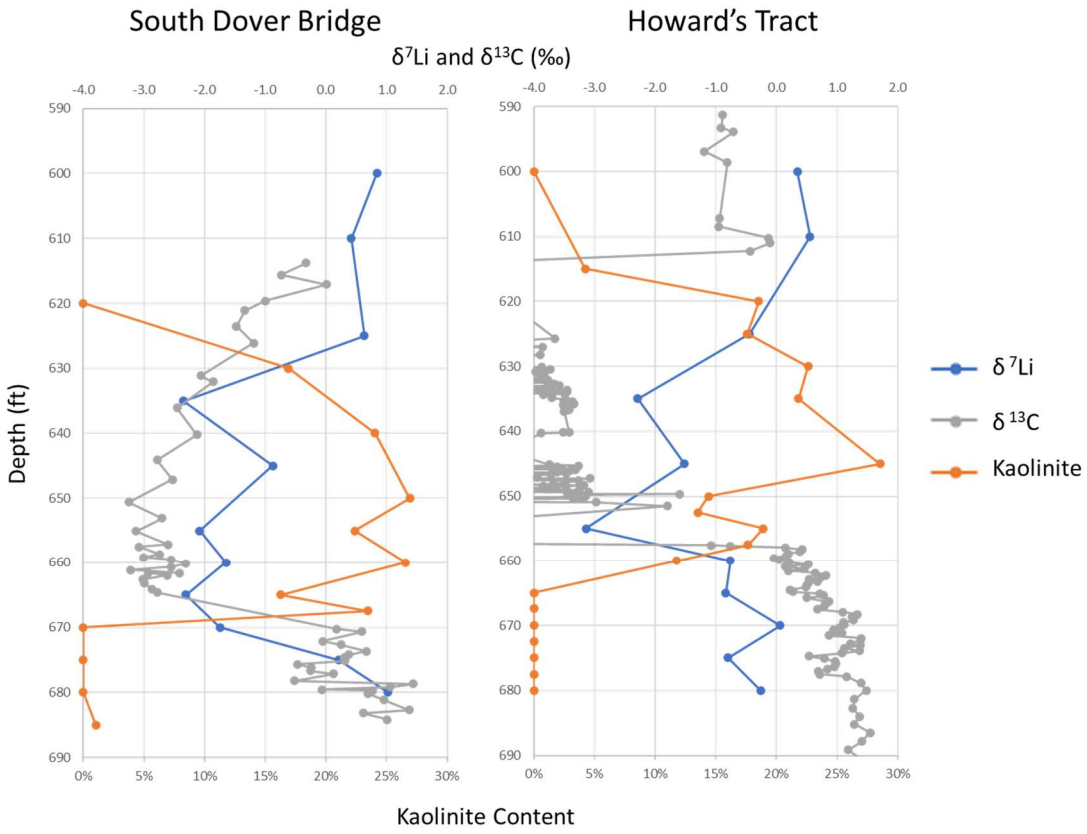

Supplemental Figure 1: $\delta^{7}Li$, bulk carbonate $\delta^{13}C$, and kaolinite content within clay sized fraction at South Dover Bridge and Howard's Tract. Note similar trends in lithium isotope composition and clay mineralogy.

REFERENCES

Abels, H.A., Lauretano, V., van Yperen, A., Hopman, T., Zachos, J.C., Lourens, L.J., Gingerich, P.D. and Bowen, G.J., 2015 Carbon isotope excursions in paleosol carbonate marking five early Eocene hyperthermals in the Bighorn Basin, Wyoming. *Clim. Past Discuss*, 11, 1857-1885. https://doi.org/10.5194/cpd-11-1857-201

Abels, H.A., Lauretano, V., Van Yperen, A.E., Hopman, T., Zachos, J.C., Lourens, L.J., Gingerich, P.D. and Bowen, G.J., 2016 Environmental impact and magnitude of paleosol carbonate carbon isotope excursions marking five early Eocene hyperthermals in the Bighorn Basin, Wyoming. *Climate of the Past*, 12(5), 1151-1163. https://doi.org/10.5194/cp-12-1151-2016

Agnini, C., Fornaciari, E., Raffi, I., Catanzariti, R., Palike, H., Backman, J., and Rio, D., 2014, Biozonation and biochronology of Paleogene calcareous nannofossils from low and middle latitudes. *Newsletters on Stratigraphy*, 47 (2), 131-181. https://doi.org/10.1127/0078-0421/2014/0042

Anderson, H. W., 1954. Suspended sediment discharge as related to streamflow, topography, soil, and land use. *Eos, Transactions American Geophysical Union*, 35(2), 268-281. https://doi.org/10.1029/TR035i002p00268

Anderson, S.P., Blum, J., Brantley, S.L., Chadwick, O., Chorover, J., Derry, L.A., Drever, J.I., Hering, J.G., Kirchner, J.W., Kump, L.R. and Richter, D., 2004. Proposed initiative would study Earth's weathering engine. *Eos, Transactions American Geophysical Union*, 85(28), pp.265-269. https://doi.org/10.1029/2004EO280001

Arakawa, A., 2004. The Cumulus Parameterization Problem: Past, Present, and Future. *Journal of Climate*, 17, 2493–2525. https://doi.org/10.1175/1520-0442(2004)017<2493:RATCPP>2.0.CO;2

Babila, T.L., Penman, D.E., Standish, C.D., Doubrawa, M., Bralower, T.J., Robinson, M.M., Self-Trail, J.M., Speijer, R.P., Stassen, P., Foster, G.L. and Zachos, J.C., 2022. Surface ocean warming and acidification driven by rapid carbon release precedes Paleocene-Eocene Thermal Maximum. *Science advances*, 8(11), p.eabg1025. https://doi.org/10.1126/sciadv.abg1025

Baxter, A.J., Hopmans, E.C., Russell, J.M. and Damsté, J.S.S., 2019. Bacterial GMGTs in East African lake sediments: Their potential as palaeotemperature indicators. *Geochimica et Cosmochimica Acta*, 259, 155-169. https://doi.org/10.1016/j.gca.2019.05.039

Bijl, P.K., Brinkhuis, H., Egger, L.M., Eldrett, J.S., Frieling, J., Grothe, A., Houben, A.J., Pross, J., Śliwińska, K.K. and Sluijs, A., 2017. Comment on 'Wetzeliella and its allies–the 'hole'story: a taxonomic revision of the Paleogene dinoflagellate subfamily Wetzelielloideae'by Williams et al.(2015). *Palynology*, 41(3), 423-429. https://doi.org/10.1080/01916122.2016.1235056

Blair, S.A. and Watkins, D.K., 2009. High-resolution calcareous nannofossil biostratigraphy for the Coniacian/Santonian Stage boundary, Western Interior Basin. *Cretaceous Research*, 30, 367-384. https://doi.org/10.1016/j.cretres.2008.07.016

Bowen, G.J., Beerling, D.J., Koch, P.L., Zachos, J.C. and Quattlebaum, T., 2004. A humid climate state during the Palaeocene/Eocene thermal maximum. *Nature*, 432(7016), 495-499. https://doi.org/10.1038/nature03115

Bown, P. and Young, J.R., 1998. Techniques. In: P.R. Bown, Ed., *Calcareous Nannofossil Biostratigraphy*, 16-28. Cambridge: Kluwer Academic Press

Bralower, T.J., Kump, L.R., Self-Trail, J.M., Robinson, M.M., Lyons, S., Babila, T., Ballaron, E., Freeman, K.H., Hajek, E., Rush, W. and Zachos, J.C., 2018. Evidence for shelf acidification during the onset of the Paleocene-Eocene thermal maximum. *Paleoceanography and Paleoclimatology*, 33(12), pp.1408-1426. https://doi.org/10.1029/2018PA003382

Brinkhuis, H., Schouten, S., Collinson, M.E., Sluijs, A., Damsté, J.S.S., Dickens, G.R., Huber, M., Cronin, T.M., Onodera, J., Takahashi, K. and Bujak, J.P., 2006. Episodic fresh surface waters in the Eocene Arctic Ocean. *Nature*, 441(7093), 606-609. https://doi.org/10.1038/nature04692

Carmichael, M.J., Pancost, R.D. and Lunt, D.J., 2018. Changes in the occurrence of extreme precipitation events at the Paleocene–Eocene thermal maximum. *Earth and Planetary Science Letters*, 501, pp.24-36. https://doi.org/10.1016/j.epsl.2018.08.005

Carmichael, M.J., Inglis, G.N., Badger, M.P., Naafs, B.D.A., Behrooz, L., Remmelzwaal, S., Monteiro, F.M., Rohrssen, M., Farnsworth, A., Buss, H.L. and Dickson, A.J., 2017. Hydrological and associated biogeochemical consequences of rapid global warming during the Paleocene-Eocene Thermal Maximum. *Global and Planetary Change*, 157, 114-138. https://doi.org/10.1016/j.gloplacha.2017.07.014

Chen, Z., Ding, Z., Yang, S., Zhang, C. and Wang, X., 2016. Increased precipitation and weathering across the Paleocene-Eocene Thermal Maximum in central China. *Geochemistry, Geophysics, Geosystems*, 17(6), pp.2286-2297. https://doi.org/10.1002/2016GC006333

Chen, C., Guerit, L., Foreman, B. Z., Hassenruck-Gudipati, H. J., Adatte, T., Honegger, L., Perret, M., Sluijs, A., Castelltort, S., 2018. Estimating regional flood discharge during Palaeocene-Eocene global warming. *Scientific reports* 8(1), 1-8. https://doi.org/10.1038/s41598-018-31076-3

Christensen, HM., 2020. Constraining stochastic parametrisation schemes using high-resolution simulations. *Quarterly Journal of the Royal Meteorological Society*, 146, 938– 962. https://doi.org/10.1002/qj.3717

Clechenko, E.R., Kelly, D.C., Harrington, G.J. and Stiles, C.A., 2007. Terrestrial records of a regional weathering profile at the Paleocene-Eocene boundary in the Williston Basin of North Dakota. *Geological Society of America Bulletin*, 119(3-4), pp.428-442. https://doi.org/10.1130/B26010.1

Cramer, B.S., Wright, J.D., Kent, D.V. and Aubry, M.P., 2003. Orbital climate forcing of δ13C excursions in the late Paleocene–early Eocene (chrons C24n–C25n). *Paleoceanography*, 18(4). https://doi.org/10.1029/2003PA000909

Cramwinckel, M. J., van der Ploeg, R., Bijl, P. K., Peterse, F., Bohaty, S. M., Röhl, U., Schouten, S., Middelburg, J. J., and Sluijs, A., 2019. Harmful algae and export

production collapse in the equatorial Atlantic during the zenith of Middle Eocene Climatic Optimum warmth, *Geology*, https://doi.org/10.1130/G45614.1

Crouch, E. M., Dickens, G. R., Brinkhuis, H., Aubry, M.-P., Hollis, C. J., Rogers, K. M., and Visscher, H., 2003. The Apectodinium acme and terrestrial discharge during the Paleocene-Eocene thermal maximum: new palynological, geochemical and calcareous nannoplankton observations at Tawanui, New Zealand, *Palaeogeography, Palaeoclimatology, Palaeoecology*, 194, 387-403 https://doi.org/10.1016/S0031-0182(03)00334-1

Dellinger, M., Gaillardet, J., Bouchez, J., Calmels, D., Louvat, P., Dosseto, A., Gorge, C., Alanoca, L. and Maurice, L., 2015. Riverine Li isotope fractionation in the Amazon River basin controlled by the weathering regimes. *Geochimica et Cosmochimica Acta*, 164, pp.71-93. https://doi.org/10.1016/j.gca.2015.04.042

Dickens, G. R., Castillo, M. M., & Walker, J. C., 1997. A blast of gas in the latest Paleocene: Simulating first-order effects of massive dissociation of oceanic methane hydrate. *Geology*, 25(3), 259-262. https://doi.org/10.1130/0091-7613(1997)025%3C0259:ABOGIT%3E2.3.CO;2

D'Onofrio, R., Luciani, V., Fornaciari, E., Giusberti, L., Boscolo Galazzo, F., Dallanave, E., Westerhold, T., Sprovieri, M. and Telch, S., 2016. Environmental perturbations at the early Eocene ETM2, H2, and I1 events as inferred by Tethyan calcareous plankton (Terche section, northeastern Italy). *Paleoceanography*, 31(9), 1225-1247. https://doi.org/10.1002/2016PA002940

Duller, R. A., Armitage, J. J., Manners, H. R., Grimes, S., Jones, T. D., 2019. Delayed sedimentary response to abrupt climate change at the Paleocene-Eocene boundary, northern Spain. *Geology* 47(2), 159-162. https://doi.org/10.1130/G45631.1

Dunkley Jones, T., Manners, H. R., Hoggett, M., Kirtland Turner, S., Westerhold, T., Leng, M. J., Pancost, R.D., Ridgwell, A., Alegret, L., Duller, R., Grimes, S.T., 2018. Dynamics of sediment flux to a bathyal continental margin section through the Paleocene–Eocene Thermal Maximum. *Climate of the Past*, 14(7), 1035-1049. https://doi.org/10.5194/cp-14-1035-2018

Eden, D. N., Page, M. J., 1998. Palaeoclimatic implications of a storm erosion record from late Holocene lake sediments, North Island, New Zealand. *Palaeogeography, Palaeoclimatology, Palaeoecology*, 139(1-2), 37-58. https://doi.org/10.1016/S0031-0182(97)00136-3

Edwards, T.W., Wolfe, B.B. and Macdonald, G.M., 1996. Influence of changing atmospheric circulation on precipitation δ18O–temperature relations in Canada during the Holocene. *Quaternary Research*, 46(3), pp.211-218. https://doi.org/10.1006/qres.1996.0061

Fairbanks, R.G., 1982. The origin of continental shelf and slope water in the New York Bight and Gulf of Maine: evidence from H2 18O/H2 16O ratio measurements. *Journal of Geophysical Research: Oceans*, 87(C8), 5796-5808. https://doi.org/10.1029/JC087iC08p057961

Frieling, J., Gebhardt, H., Huber, M., Adekeye, O. A., Akande, S. O., Reichart, G.-J., Middelburg, J. J., Schouten, S., and Sluijs, A., 2017. Extreme warmth and heat-stressed plankton in the tropics during the Paleocene-Eocene Thermal Maximum, *Science Advances*, 3, e1600891, https://doi.org/10.1126/sciadv.1600891

Frieling, J., Peterse, F., Lunt, D.J., Bohaty, S.M., Sinninghe Damsté, J.S., Reichart, G.J. and Sluijs, A., 2019. Widespread warming before and elevated barium burial during the Paleocene-Eocene Thermal Maximum: Evidence for methane hydrate release?. *Paleoceanography and paleoclimatology*, 34(4), 546-566

Frieling, J. and Sluijs, A., 2018. Towards quantitative environmental reconstructions from ancient non-analogue microfossil assemblages: Ecological preferences of Paleocene–Eocene dinoflagellates. *Earth-Science Reviews*, 185, 956-973. https://doi.org/10.1016/j.earscirev.2018.08.014

Gibson, T.G., Bybell, L.M., Mason, D.B., 2000, Stratigraphic and climatic implications of clay mineral changes around the Paleocene/Eocene boundary of the northeastern US margin. Sedimentary *Geology*, 134(1-2), 65-92. https://doi.org/10.1016/S0037-0738(00)00014-2

Golla, J.K., Kuessner, M.L., Henehan, M.J., Bouchez, J., Rempe, D.M. and Druhan, J.L., 2021. The evolution of lithium isotope signatures in fluids draining actively weathering hillslopes. *Earth and Planetary Science Letters*, 567, p.116988. https://doi.org/10.1016/j.epsl.2021.116988

Guenther, A. B., Jiang, X., Heald, Colette L., Sakulyanontvittaya, T., Duhl, T., Emmons, L. K., Wang, X., 2012. The Model of Emissions of Gases and Aerosols from Nature version 2.1 (MEGAN2. 1): an extended and updated framework for modeling biogenic emissions. *Geoscientific Model Development*, 5, 1471–1492. https://doi.org/10.5194/gmd-5-1471-2012

Gutjahr, M., Ridgwell, A., Sexton, P. F., Anagnostou, E., Pearson, P. N., Pälike, H., Norris, R.D., Thomas, E., Foster, G.L., 2017, Very large release of mostly volcanic carbon during the Palaeocene–Eocene Thermal Maximum. *Nature* 548(7669), 573-577. https://doi.org/10.1038/nature23646

Handley, L., O'Halloran, A., Pearson, P. N., Hawkins, E., Nicholas, C. J., Schouten, S., McMillan, I.K., Pancost, R.D., 2012. Changes in the hydrological cycle in tropical East Africa during the Paleocene–Eocene Thermal Maximum. *Palaeogeography, Palaeoclimatology, Palaeoecology*, 329, 10-21. https://doi.org/10.1016/j.palaeo.2012.02.002

Harper, D. T., Hönisch, B., Zeebe, R. E., Shaffer, G., Haynes, L. L., Thomas, E., & Zachos, J. C., 2020. The magnitude of surface ocean acidification and carbon release during Eocene Thermal Maximum 2 (ETM-2) and the Paleocene-Eocene Thermal Maximum (PETM). *Paleoceanography and Paleoclimatology*, 35(2), e2019PA003699. https://doi.org/10.1029/2019PA003699

Harper, D.T., Zeebe, R., Hönisch, B., Schrader, C.D., Lourens, L.J. and Zachos, J.C., 2018. Subtropical sea-surface warming and increased salinity during Eocene Thermal Maximum 2. *Geology*, 46(2), 187-190. https://doi.org/10.1130/G39658.1

Held, I.M., Soden, B.J., 2006. Robust responses of the hydrological cycle to global warming. *Journal of Climate*, 19(21), 5686-5699. https://doi.org/10.1175/JCLI3990.1

Ho, S. L. and Laepple, T., 2016. Flat meridional temperature gradient in the early Eocene in the subsurface rather than surface ocean, *Nature Geoscience*, 9(August), https://doi.org/10.1038/ngeo2763

Hollis, C.J., Dunkley Jones, T., Anagnostou, E., Bijl, P.K., Cramwinckel, M.J., Cui, Y., Dickens, G.R., Edgar, K.M., Eley, Y., Evans, D. and Foster, G.L., 2019. The DeepMIP contribution to PMIP4: methodologies for selection, compilation and analysis of latest Paleocene and early Eocene climate proxy data, incorporating version 0.1 of the DeepMIP database. *Geoscientific Model Development*, 12(7), 3149-3206. https://doi.org/10.5194/gmd-12-3149-2019

Hopmans, E.C., Schouten, S. and Damsté, J.S.S., 2016. The effect of improved chromatography on GDGT-based palaeoproxies. *Organic Geochemistry*, 93, 1-6. https://doi.org/10.1016/j.orggeochem.2015.12.006

Hurley, S. J., Lipp, J. S., Close, H. G., Hinrichs, K. U. and Pearson, A., 2018. Distribution and export of isoprenoid tetraether lipids in suspended particulate matter from the water column of the Western Atlantic Ocean, *Organic Geochemistry*, 116, 90–102, https://doi.org/10.1016/j.orggeochem.2017.11.010

Jackson, L.C., Kahana, R., Graham, T., Ringer, M.A., Woollings, T., Mecking, J.V. and Wood, R.A., 2015. Global and European climate impacts of a slowdown of the AMOC in a high resolution GCM. *Climate dynamics*, 45(11), 3299-3316. https://doi.org/10.1007/s00382-015-2540-2

Jakob, C., 2010. Accelerating Progress in Global Atmospheric Model Development through Improved Parameterizations: Challenges, Opportunities, and Strategies. *Bulletin of the American Meteorological Society*, 91, 869-875. https://doi.org/10.1175/2009BAMS2898.1

Jiang, J., Hu, X., Li, J., BouDagher-Fadel, M., & Garzanti, E., 2021. Discovery of the Paleocene-Eocene Thermal Maximum in shallow-marine sediments of the Xigaze forearc basin, Tibet: A record of enhanced extreme precipitation and siliciclastic sediment flux. *Palaeogeography, Palaeoclimatology, Palaeoecology*, 562, 110095. https://doi.org/10.1016/j.palaeo.2020.110095

Jin, S., Kemp, D.B., Jolley, D.W., Vieira, M., Zachos, J.C., Huang, C., Li, M. and Chen, W., 2022. Large-scale, astronomically paced sediment input to the North Sea Basin during the Paleocene Eocene Thermal Maximum. *Earth and Planetary Science Letters*, 579, 117340. https://doi.org/10.1016/j.epsl.2021.117340

John, C. M., Banerjee, N. R., Longstaffe, F. J., Sica, C., Law, K. R., Zachos, J. C., 2012. Clay assemblage and oxygen isotopic constraints on the weathering response to the Paleocene-Eocene thermal maximum, east coast of North America. *Geology*, 40(7), 591-594 https://doi.org/10.1130/G32785.1

John, C. M., Bohaty, S. M., Zachos, J. C., Sluijs, A., Gibbs, S., Brinkhuis, H., Bralower, T. J., 2008. North American continental margin records of the Paleocene-Eocene thermal maximum: Implications for global carbon and hydrological cycling. *Paleoceanography*, 23(2). https://doi.org/10.1029/2007PA001465

Kemp, S.J., Ellis, M.A., Mounteney, I. and Kender, S., 2016, Palaeoclimatic implications of high-resolution clay mineral assemblages preceding and across the onset of the Palaeocene–Eocene Thermal Maximum, North Sea Basin. *Clay Minerals*, 51(5), pp.793-813. https://doi.org/10.1180/claymin.2016.051.5.08

Kiehl, J. T., Shields, C. A., Snyder, M. A., Zachos, J. C., Rothstein, M., 2018. Greenhouse-and orbital-forced climate extremes during the early Eocene. *Philosophical Transactions of the Royal Society A: Mathematical, Physical and Engineering Sciences*, 376(2130), 20170085. https://doi.org/10.1098/rsta.2017.0085

Kiehl, J. T., Zarzycki, C. M., Shields, C. A., Rothstein, M. V., In review. Simulated Changes to Tropical Cyclones Across the Paleocene Eocene Thermal Maximum (PETM) Boundary. *Palaeogeography, Palaeoclimatology, Palaeoecology*

Kim, J.H., Van der Meer, J., Schouten, S., Helmke, P., Willmott, V., Sangiorgi, F., Koç, N., Hopmans, E.C. and Damsté, J.S.S., 2010. New indices and calibrations derived from the distribution of crenarchaeal isoprenoid tetraether lipids: Implications for past sea surface temperature reconstructions. *Geochimica et Cosmochimica Acta*, 74(16), 4639-4654. https://doi.org/10.1016/j.gca.2010.05.027

Kopp, R.E., Schumann, D., Raub, T.D., Powars, D.S., Godfrey, L.V., Swanson-Hysell, N.L., Maloof, A.C. and Vali, H., 2009. An Appalachian Amazon? Magnetofossil evidence for the development of a tropical river-like system in the

mid-Atlantic United States during the Paleocene-Eocene thermal maximum. *Paleoceanography*, 24(4). https://doi.org/10.1029/2009PA001783

Krishnan, S., Pagani, M., Huber, M. and Sluijs, A., 2014. High latitude hydrological changes during the Eocene Thermal Maximum 2. *Earth and Planetary Science Letters*, 404, 167-177. https://doi.org/10.1016/j.epsl.2014.07.029

Laing, A., & Evans, J. L., 2011. *Introduction to tropical meteorology*. Educational material from The COMET Program.

Langbein, W. B., Schumm, S. A., 1958. Yield of sediment in relation to mean annual precipitation. *Eos, Transactions American Geophysical Union*, 39(6), 1076-1084. https://doi.org/10.1029/TR039i006p01076

Lauretano, V., Littler, K., Polling, M., Zachos, J.C. and Lourens, L.J., 2015. Frequency, magnitude and character of hyperthermal events at the onset of the Early Eocene Climatic Optimum. *Climate of the Past*, 11(10), 1313-1324. https://doi.org/10.1029/2018PA003422

Lawrence, D. M., Oleson, K. W., Flanner, M. G., Thornton, P. E., Swenson, S. C., Lawrence, P. J., Zeng, X., Yang, Z.L., Levis, S., Sakaguchi, K., Bonan, G.B., 2011. Parameterization improvements and functional and structural advances in version 4 of the community land model. *Journal of Advances in Modeling Earth Systems*, 3(1). https://doi.org/10.1029/2011MS00045

Lippert, P. C., Zachos, J. C., 2007. A biogenic origin for anomalous fine-grained magnetic material at the Paleocene-Eocene boundary at Wilson Lake, New Jersey. *Paleoceanography*, 22(4). https://doi.org/10.1029/2007PA001471

Liu, X.M., Wanner, C., Rudnick, R.L. and McDonough, W.F., 2015. Processes controlling δ7Li in rivers illuminated by study of streams and groundwaters draining basalts. *Earth and Planetary Science Letters*, 409, pp.212-224. https://doi.org/10.1016/j.epsl.2014.10.032

Lyons, S.L., Baczynski, A.A., Babila, T.L., Bralower, T.J., Hajek, E.A., Kump, L.R., Polites, E.G., Self-Trail, J.M., Trampush, S.M., Vornlocher, J.R. and Zachos, J.C., 2019. Palaeocene–Eocene thermal maximum prolonged by fossil carbon oxidation. *Nature Geoscience*, 12(1), pp.54-60. https://doi.org/10.1038/s41561-018-0277-3

Lunt, D. J., Huber, M., Anagnostou, E., Baatsen, M. L. J., Caballero, R., DeConto, R., Dijkstra, H.A., Donnadieu, Y., Evans, D., Feng, R., Foster, G.L., 2017. The DeepMIP contribution to PMIP4: experimental design for model simulations of the EECO, PETM, and pre-PETM (version 1.0). *Geoscientific Model Development*, 10, 889–901. https://doi.org/10.5194/gmd-10-889-2017

Littler, K., Röhl, U., Westerhold, T., Zachos, J.C., 2014. A high-resolution benthic stable-isotope record for the South Atlantic: Implications for orbital-scale changes in Late Paleocene–Early Eocene climate and carbon cycling. *Earth and Planetary Science Letters*, 401, 18-30. https://doi.org/10.1016/j.epsl.2014.05.054

Liu, X.L., Summons, R.E. and Hinrichs, K.U., 2012. Extending the known range of glycerol ether lipids in the environment: structural assignments based on tandem mass spectral fragmentation patterns. *Rapid Communications in Mass Spectrometry*, 26(19), 2295-2302. https://doi.org/10.1002/rcm.6355

Lourens, L.J., Sluijs, A., Kroon, D., Zachos, J.C., Thomas, E., Röhl, U., Bowles, J. and Raffi, I., 2005. Astronomical pacing of late Palaeocene to early Eocene global warming events. *Nature*, 435(7045), 1083-1087. https://doi.org/10.1038/nature03814

Marchitto, T.M., Curry, W.B., Lynch-Stieglitz, J., Bryan, S.P., Cobb, K.M. and Lund, D.C., 2014. Improved oxygen isotope temperature calibrations for cosmopolitan benthic foraminifera. *Geochimica et Cosmochimica Acta*, 130, 1-11. https://doi.org/10.1016/j.gca.2013.12.034

Martini, W., 1971. Standard Tertiary and Quaternary calcareous nannoplankton zonation. In: Farinacci, A., Ed., Proceedings of the 2nd Planktonic Conference, Roma, 2: 739-785

Masson-Delmotte, V., P. Zhai, A. Pirani, S.L. Connors, C. Péan, S. Berger, N. Caud, Y. Chen, L. Goldfarb, M.I. Gomis, M. Huang, K. Leitzell, E. Lonnoy, J.B.R. Matthews, T.K. Maycock, T. Waterfield, O. Yelekçi, R. Yu, and Zhou, B.: IPCC, 2021: Climate Change 2021: The Physical Science Basis. Contribution of Working Group I to the Sixth Assessment Report of the Intergovernmental Panel on Climate Change. Cambridge University Press. In Press.

McFarlane, N., 2011. Parameterizations: representing key processes in climate models without resolving them. *Wiley Interdisciplinary Reviews: Climate Change*, 2, 482-497. https://doi.org/10.1002/wcc.122

McInerney, F. A., Wing, S. L., 2011. The Paleocene-Eocene Thermal Maximum: a perturbation of carbon cycle, climate, and biosphere with implications for the future. *Annual Review of Earth and Planetary Sciences*, 39, 489-516. https://doi.org/10.1146/annurev-earth-040610-133431

Miller, K.G., Kominz, M.A., Browning, J.V., Wright, J.D., Mountain, G.S., Katz, M.E., Sugarman, P.J., Cramer, B.S., Christie-Blick, N. and Pekar, S.F., 2005. The Phanerozoic record of global sea-level change. *Science*, 310(5752), 1293-1298. https://doi.org/10.1126/science.1116412

Molnar, P., 2001. Climate change, flooding in arid environments, and erosion rates. *Geology*, 29(12), 1071-1074. https://doi.org/10.1130/0091-7613(2001)029<1071:CCFIAE>2.0.CO;2

Naafs, B.D.A., Rohrssen, M., Inglis, G.N., Lähteenoja, O., Feakins, S.J., Collinson, M.E., Kennedy, E.M., Singh, P.K., Singh, M.P., Lunt, D.J. and Pancost, R.D., 2018. High temperatures in the terrestrial mid-latitudes during the early Palaeogene. *Nature Geoscience*, 11(10), 766-771. https://doi.org/10.1038/s41561-018-0199-0

National Research Council, 2001. Basic research opportunities in earth science.

Neale, R. B., Chen, C. C., Gettelman, A., Lauritzen, P. H., Park, S., Williamson, D. L., Conley, A.J., Garcia, R., Kinnison, D., Lamarque, J.F., Marsh, D., 2010.

Description of the NCAR community atmosphere model (CAM5.0). *NCAR Technical Reports*, NCAR/TN-486+STR 1-12.

Nearing, M.A., Jetten, V., Baffaut, C., Cerdan, O., Couturier, A., Hernandez, M., Le Bissonnais, Y., Nichols, M.H., Nunes, J.P., Renschler, C.S. and Souchère, V., 2005. Modeling response of soil erosion and runoff to changes in precipitation and cover. *Catena*, 61(2-3), pp.131-154.

Nicolo, M.J., Dickens, G.R., Hollis, C.J. and Zachos, J.C., 2007. Multiple early Eocene hyperthermals: Their sedimentary expression on the New Zealand continental margin and in the deep sea. *Geology*, 35(8), 699-702. https://doi.org/10.1130/G23648A.1

O'Brien, C.L., Robinson, S.A., Pancost, R.D., Damsté, J.S.S., Schouten, S., Lunt, D.J., Alsenz, H., Bornemann, A., Bottini, C., Brassell, S.C. and Farnsworth, A., 2017. Cretaceous sea-surface temperature evolution: Constraints from TEX86 and planktonic foraminiferal oxygen isotopes. *Earth-Science Reviews*, 172, 224-247. https://doi.org/10.1016/j.earscirev.2017.07.012

O'Gorman, P. A., 2010. Understanding the varied response of the extratropical storm tracks to climate change. *Proceedings of the National Academy of Sciences*, 107(45), 19176-19180. https://doi.org/10.1073/pnas.1011547107

Park, S., Bretherton, C. S., Rasch, P. J., 2014. Integrating cloud processes in the community atmosphere model, Version 5. *Journal of Climate*, 27, 6821–6856. https://doi.org/10.1175/JCLI-D-14-00087.1

Pfahl, S., O'Gorman, P. A., Fischer, E. M., 2017. Understanding the regional pattern of projected future changes in extreme precipitation. *Nature Climate Change*, 7(6), 423-427. https://doi.org/10.1038/nclimate3287

Pistiner, J.S. and Henderson, G.M., 2003. Lithium-isotope fractionation during continental weathering processes. *Earth and Planetary Science Letters*, 214(1-2), pp.327-339. https://doi.org/10.1016/S0012-821X(03)00348-0

Pogge von Strandmann, P.A., Jenkyns, H.C. and Woodfine, R.G., 2013. Lithium isotope evidence for enhanced weathering during Oceanic Anoxic Event 2. *Nature Geoscience*, 6(8), pp.668-672. https://doi.org/10.1038/ngeo1875

Pogge von Strandmann, P.A., Jones, M.T., West, A.J., Murphy, M.J., Stokke, E.W., Tarbuck, G., Wilson, D.J., Pearce, C.R. and Schmidt, D.N., 2021. Lithium isotope evidence for enhanced weathering and erosion during the Paleocene-Eocene Thermal Maximum. *Science advances*, 7(42), p.eabh4224. https://doi.org/10.1126/sciadv.abh4224

Poppe, L.J., Paskevich, V.F., Hathaway, J.C. and Blackwood, D.S., 2001, A laboratory manual for X-ray powder diffraction. US Geological Survey open-file report, 1(041), pp.1-88.

Pross, J. and Brinkhuis, H., 2005. Organic-walled dinoflagellate cysts as paleoenvironmental indicators in the Paleogene; a synopsis of concepts. *Paläontologische Zeitschrift*, 79(1), 53-59. https://doi.org/10.1007/BF03021753

Pujalte, V., Baceta, J. I., Schmitz, B., 2015. A massive input of coarse-grained siliciclastics in the Pyrenean Basin during the PETM: the missing ingredient in a coeval abrupt change in hydrological regime. *Climate of the Past*, 11(12). https://doi.org/10.5194/cp-11-1653-2015

Pujalte, V., Schmitz, B., 2014. Comment on" Magnitude and profile of organic carbon isotope records from the Paleocene-Eocene Thermal Maximum: Evidence from northern Spain" by Manners et al.[Earth Planet. Sci. Lett. 376 (2013) 220-230]. *Earth and Planetary Science Letters*, 395, 291-293. https://doi.org/10.1016/j.epsl.2014.03.054

Ralph, F. M., 2019. *Atmospheric Rivers*. Springer Nature.

Ramos, E.J., Breecker, D.O., Barnes, J.D., Li, F., Gingerich, P.D., Loewy, S.L., Satkoski, A.M., Baczynski, A.A., Wing, S.L., Miller, N.R. and Lassiter, J.C., 2022. Swift weathering response on floodplains during the Paleocene-Eocene Thermal Maximum. *Geophysical Research Letters*, p.e2021GL097436. https://doi.org/10.1029/2021GL097436

Reichart, G.J., Brinkhuis, H., Huiskamp, F. and Zachariasse, W.J., 2004. Hyperstratification following glacial overturning events in the northern Arabian Sea. *Paleoceanography*, 19(2). https://doi.org/10.1029/2003PA000900

Reinhardt, L., von Gosen, W., Lückge, A., Blumenberg, M., Galloway, J.M., West, C.K., Sudermann, M. and Dolezych, M., 2022. Geochemical indications for the Paleocene-Eocene Thermal Maximum (PETM) and Eocene Thermal Maximum 2 (ETM-2) hyperthermals in terrestrial sediments of the Canadian Arctic. *Geosphere*. https://doi.org/10.1130/GES02398.1

Reynolds, P., Planke, S., Millett, J. M., Jerram, D. A., Trulsvik, M., Schofield, N., & Myklebust, R., 2017. Hydrothermal vent complexes offshore Northeast Greenland: A potential role in driving the PETM. *Earth and Planetary Science Letters*, 467, 72-78. https://doi.org/10.1016/j.epsl.2017.03.031

Richaud, B., Kwon, Y.O., Joyce, T.M., Fratantoni, P.S. and Lentz, S.J., 2016. Surface and bottom temperature and salinity climatology along the continental shelf off the Canadian and US East Coasts. *Continental Shelf Research*, 124, 165-181. https://doi.org/10.1016/j.csr.2016.06.005

Riebe, C.S., Hahm, W.J. and Brantley, S.L., 2017. Controls on deep critical zone architecture: A historical review and four testable hypotheses. *Earth Surface Processes and Landforms*, 42(1), pp.128-156. https://doi.org/10.1002/esp.4052

Robert, C. and Kennett, J.P., 1994. Antarctic subtropical humid episode at the Paleocene-Eocene boundary: Clay-mineral evidence. *Geology*, 22(3), pp.211-214. https://doi.org/10.1130/0091-7613(1994)022%3C0211:ASHEAT%3E2.3.CO;2

Robert, C., Kennett, J. P., 1994. Antarctic subtropical humid episode at the Paleocene-Eocene boundary: Clay-mineral evidence. *Geology*, 22(3), 211-214. https://doi.org/10.1130/0091-7613(1994)022<0211:ASHEAT>2.3.CO;2

Rossi, M. W., Whipple, K. X., Vivoni, E. R., 2016. Precipitation and evapotranspiration controls on daily runoff variability in the contiguous United States and Puerto Rico. *Journal of Geophysical Research: Earth Surface*, 121(1), 128-145. https://doi.org/10.1002/2015JF003446

Rush, W.D., Kiehl, J.T., Shields, C.A. and Zachos, J.C., 2021. Increased frequency of extreme precipitation events in the North Atlantic during the PETM: Observations and theory. *Palaeogeography, Palaeoclimatology, Palaeoecology*, 568, p.110289. https://doi.org/10.1016/j.palaeo.2021.110289

Savin, S.M. and Epstein, S., 1970. The oxygen and hydrogen isotope geochemistry of clay minerals. *Geochimica et Cosmochimica Acta*, 34(1), pp.25-42. https://doi.org/10.1016/0016-7037(70)90149-3

Schmitz, B., Pujalte, V., 2007. Abrupt increase in seasonal extreme precipitation at the Paleocene-Eocene boundary. *Geology*, 35(3), 215-218. https://doi.org/10.1130/G23261A.1

Schmitz, B., Pujalte, V., Nunez-Betelu, K., 2001. Climate and sea-level perturbations during the Incipient Eocene Thermal Maximum: evidence from siliciclastic units in the Basque Basin (Ermua, Zumaia and Trabakua Pass), northern Spain. *Palaeogeography, Palaeoclimatology, Palaeoecology*, 165(3-4), 299-320. https://doi.org/10.1016/S0031-0182(00)00167-X

Schouten, S., Hopmans, E.C. and Damsté, J.S.S., 2013. The organic geochemistry of glycerol dialkyl glycerol tetraether lipids: A review. *Organic geochemistry*, 54, 19-61. https://doi.org/10.1016/j.orggeochem.2012.09.006

Schouten, S., Hopmans, E.C., Schefuß, E. and Damste, J.S.S., 2002. Distributional variations in marine crenarchaeotal membrane lipids: a new tool for reconstructing ancient sea water temperatures?. *Earth and Planetary Science Letters*, 204(1-2), 265-274. https://doi.org/10.1016/S0012-821X(02)00979-2

Self-Trail, J.M., Powars, D.S., Watkins, D.K. and Wandless, G.A., 2012. Calcareous nannofossil assemblage changes across the Paleocene–Eocene Thermal Maximum: Evidence from a shelf setting. *Marine Micropaleontology*, 92, 61-80. https://doi.org/10.1016/j.marmicro.2012.05.003

Self-Trail, J. M., Robinson, M. M., Bralower, T. J., Sessa, J. A., Hajek, E. A., Kump, L. R., Trampush, S.M., Willard, D.A., Edwards, L.E., Powars, D.S., Wandless, G.A., 2017. Shallow marine response to global climate change during the Paleocene-Eocene Thermal Maximum, Salisbury Embayment, USA. *Paleoceanography*, 32(7), 710-728. https://doi.org/10.1002/2017PA003096

Shields, C. A., Kiehl, J. T., Rush, W. D., Rothstein, M., Snyder, M. A., In review. Atmospheric rivers in high-resolution simulations of the Paleocene Eocene Thermal Maximum (PETM). *Palaeogeography, Palaeoclimatology, Palaeoecology*

Singer, A., 1980. The paleoclimatic interpretation of clay minerals in soils and weathering profiles. *Earth-Science Reviews*, 15(4), 303-326. https://doi.org/10.1016/0012-8252(80)90113-0

Slotnick, B.S., Dickens, G.R., Nicolo, M.J., Hollis, C.J., Crampton, J.S., Zachos, J.C. and Sluijs, A., 2012. Large-amplitude variations in carbon cycling and terrestrial weathering during the latest Paleocene and earliest Eocene: The record at Mead Stream, New Zealand. *The Journal of Geology*, 120(5), 487-505. https://doi.org/10.1086/666743

Sluijs, A., Brinkhuis, H., Schouten, S., Bohaty, S.M., John, C.M., Zachos, J.C., Reichart, G.J., Damste, J.S.S., Crouch, E.M. and Dickens, G.R., 2007. Environmental precursors to rapid light carbon injection at the Palaeocene/Eocene boundary. *Nature*, 450(7173), 1218-1221. https://doi.org/10.1038/nature06400

Sluijs, A., Brinkhuis, H., 2009. A dynamic climate and ecosystem state during the Paleocene-Eocene Thermal Maximum: inferences from dinoflagellate cyst assemblages on the New Jersey Shelf. *Biogeosciences*, 6(8), 1755-1781. https://doi.org/10.5194/bg-6-1755-2009

Sluijs, A. and Dickens, G.R., 2012. Assessing offsets between the δ13C of sedimentary components and the global exogenic carbon pool across early Paleogene carbon cycle perturbations. *Global Biogeochemical Cycles*, 26(4). https://doi.org/10.1029/2011GB004224

Sluijs, A., Pross, J. and Brinkhuis, H., 2005. From greenhouse to icehouse; organic-walled dinoflagellate cysts as paleoenvironmental indicators in the Paleogene. *Earth-Science Reviews*, 68(3-4), 281-315. https://doi.org/10.1016/j.earscirev.2004.06.001

Sluijs, A., Schouten, S., Donders, T.H., Schoon, P.L., Röhl, U., Reichart, G.J., Sangiorgi, F., Kim, J.H., Sinninghe Damsté, J.S. and Brinkhuis, H., 2009. Warm and wet conditions in the Arctic region during Eocene Thermal Maximum 2. *Nature Geoscience*, 2(11), 777-780. https://doi.org/10.1038/ngeo668

Sluijs, A., van Roij, L., Frieling, J., Laks, J., and Reichart, G.J., 2018. Single-species dinoflagellate cyst carbon isotope ecology across the Paleocene-Eocene Thermal Maximum, *Geology*, 46, 79-82. https://doi.org/10.1130/G39598.1

Sluijs, A., Van Roij, L., Harrington, G.J., Schouten, S., Sessa, J.A., LeVay, L.J., Reichart, G.J. and Slomp, C.P., 2014. Warming, euxinia and sea level rise during the Paleocene–Eocene Thermal Maximum on the Gulf Coastal Plain: implications for ocean oxygenation and nutrient cycling. *Climate of the Past*, 10(4), 1421-1439. https://doi.org/10.5194/cp-10-1421-2014

Speijer, R.P., Pälike, H., Hollis, C.J., Hooker, J.J., Ogg, J.G., 2020. Chapter 28 - The Paleogene Period, Editor(s): Felix M. Gradstein, James G. Ogg, Mark D. Schmitz, Gabi M. Ogg, Geologic Time Scale 2020, Elsevier, 1087-1140, ISBN 9780128243602, https://doi.org/10.1016/B978-0-12-824360-2.00028-0

Stap, L., Lourens, L.J., Thomas, E., Sluijs, A., Bohaty, S. and Zachos, J.C., 2010. High-resolution deep-sea carbon and oxygen isotope records of Eocene Thermal Maximum 2 and H2. *Geology*, 38(7), 607-610. https://doi.org/10.1130/G30777.1

Stassen, P., Steurbaut, E., Morsi, A.M., Schulte, P. and Speijer, R., 2012. Biotic impact of Eocene Thermal Maximum 2 in a shelf setting (Dababiya, Egypt). *Austrian Journal of Earth Sciences*, 105(1), 154-160

Stassen, P., Thomas, E., Speijer, R. P., 2012. Integrated stratigraphy of the Paleocene-Eocene thermal maximum in the New Jersey Coastal Plain: Toward understanding the effects of global warming in a shelf environment. *Paleoceanography*, 27(4). https://doi.org/10.1029/2012PA002323

Swain, D.L., Langenbrunner, B., Neelin, J.D. and Hall, A., 2018. Increasing precipitation volatility in twenty-first-century California. *Nature Climate Change*, 8(5), 427-433. https://doi.org/10.1038/s41558-018-0140-y

Tessier, A.P.G.C., Campbell, P.G. and Bisson, M.J.A.C., 1979. Sequential extraction procedure for the speciation of particulate trace metals. *Analytical chemistry*, 51(7), pp.844-851.

Thiry, M., 2000. Palaeoclimatic interpretation of clay minerals in marine deposits: an outlook from the continental origin. *Earth-Science Reviews*, 49(1-4), pp.201-221. https://doi.org/10.1016/S0012-8252(99)00054-9

Thornburg, J.D., Miller, K.G., Browning, J.V. and Wright, J.D., 2019. Mid-Cretaceous Paleopedology and Landscape Reconstruction of the Mid-Atlantic US Coastal Plain. *Journal of Sedimentary Research*, 89(4), pp.253-272. https://doi.org/10.2110/jsr.2019.12

Tipple, B.J., Pagani, M., Krishnan, S., Dirghangi, S.S., Galeotti, S., Agnini, C., Giusberti, L. and Rio, D., 2011. Coupled high-resolution marine and terrestrial

records of carbon and hydrologic cycles variations during the Paleocene–Eocene Thermal Maximum (PETM). *Earth and Planetary Science Letters*, 311(1-2), 82-92. https://doi.org/10.1016/j.epsl.2011.08.045

Trampush, S.M. and Hajek, E.A., 2017. Preserving proxy records in dynamic landscapes: Modeling and examples from the Paleocene-Eocene Thermal Maximum. *Geology*, 45(11), 967-970. https://doi.org/doi:10.1130/G39367.1

van der Weijst, C. M. H., van der Laan, K. J., Peterse, F., Reichart, G.-J., Sangiorgi, F., Schouten, S., Veenstra, T. J. T., and Sluijs, A., 2021. A fifteen-million-year surface- and subsurface-integrated TEX86 temperature record from the eastern equatorial Atlantic, *Climates of the Past Discussions* [preprint], https://doi.org/10.5194/cp-2021-92, in review

Van Hinsbergen, D. J. J., de Groot, L. V., van Schaik, S. J., Spakman, W., Bijl, P. K., Sluijs, A., Langereis, C. G., and Brinkhuis, H., 2015. A Paleolatitude Calculator for Paleoclimate Studies, *PLOS ONE*, 10, e0126946, https://doi.org/10.1371/journal.pone.0126946

Westerhold, T., Röhl, U., Laskar, J., Raffi, I., Bowles, J., Lourens, L.J. and Zachos, J.C., 2007. On the duration of magnetochrons C24r and C25n and the timing of early Eocene global warming events: Implications from the Ocean Drilling Program Leg 208 Walvis Ridge depth transect. *Paleoceanography*, 22(2). https://doi.org/10.1029/2006PA001322

Williams, G.L., Damassa, S.P., Fensome, R.A. and Guerstein, G.R., 2017. A response to 'Comment to Wetzeliella and its allies–the 'hole'story: a taxonomic revision of the

Paleogene dinoflagellate subfamily Wetzelielloideae by Williams et al.(2015)'. *Palynology*, 41(3), 430-437. https://doi.org/10.1080/01916122.2017.1283367

Zachos, J. C., Dickens, G. R., and Zeebe, R. E., 2008. An early Cenozoic perspective on greenhouse warming and carbon-cycle dynamics. *Nature* 451, no. 7176 (2008): 279-283. https://doi.org/10.1038/nature06588

Zachos, J.C., Röhl, U., Schellenberg, S.A., Sluijs, A., Hodell, D.A., Kelly, D.C., Thomas, E., Nicolo, M., Raffi, I., Lourens, L.J. and McCarren, H., 2005. Rapid acidification of the ocean during the Paleocene-Eocene thermal maximum. *Science*, 308(5728), pp.1611-1615. https://doi.org/10.1126/science.1109004

Zachos, J.C., Schouten, S., Bohaty, S., Quattlebaum, T., Sluijs, A., Brinkhuis, H., Gibbs, S.J., and Bralower, T.J., 2006. Extreme warming of mid-latitude coastal ocean during the Paleocene-Eocene Thermal Maximum: Inferences from TEX86 and isotope data: *Geology*, v. 34, 737–740, https://doi.org/10.1130/G22522.1

Zachos, J. C., McCarren, H., Murphy, B., Röhl, U., & Westerhold, T., 2010. Tempo and scale of late Paleocene and early Eocene carbon isotope cycles: Implications for the origin of hyperthermals. *Earth and Planetary Science Letters*, 299(1-2), 242-249

Zeebe, R. E., Lourens, L. J., 2019. Solar System chaos and the Paleocene–Eocene boundary age constrained by geology and astronomy. *Science*, 365(6456), 926-929. https://doi.org/10.1126/science.aax0612

Zeebe, R. E., Westerhold, T., Littler, K., and Zachos, J. C., 2017. Orbital forcing of the Paleocene and Eocene carbon cycle, *Paleoceanography*, 32, 440-465, https://doi.org/10.1002/2016PA003054

Zeebe, R. E., Zachos, J. C., 2013. Long-term legacy of massive carbon input to the Earth system: Anthropocene versus Eocene. *Philosophical Transactions of the Royal Society A: Mathematical, Physical and Engineering Sciences*, 371(2001), 20120006. https://doi.org/10.1098/rsta.2012.0006

Zeebe, R.E., Zachos, J.C., Dickens, G.R., 2009. Carbon dioxide forcing alone insufficient to explain Palaeocene–Eocene Thermal Maximum warming. *Nature Geoscience*, 2(8), 576-580. https://doi.org/10.1038/ngeo578

Zonneveld, K.A., Marret, F., Versteegh, G.J., Bogus, K., Bonnet, S., Bouimetarhan, I., Crouch, E., de Vernal, A., Elshanawany, R., Edwards, L. and Esper, O., 2013. Atlas of modern dinoflagellate cyst distribution based on 2405 data points. *Review of Palaeobotany and Palynology*, 191, 1-197. https://doi.org/10.1016/j.revpalbo.2012.08.003